

# **Investigation of Flame Stabilization in a Dual-Mode Scramjet Combustor using a Pulsed Nanosecond Discharge**

---

A

## **Thesis**

Presented to  
the faculty of the School of Engineering and Applied Science  
University of Virginia

---

in partial fulfillment  
of the requirements for the degree

Master of Science in Mechanical and Aerospace Engineering

by

Steven J. Stine

May 2025

**CLEARED**  
**For Open Publication**

Dec 17, 2024

Department of Defense  
OFFICE OF PREPUBLICATION AND SECURITY REVIEW

**DISTRIBUTION A.** Approved for public release: distribution is unlimited.



## Approval Sheet

This

### **Thesis**

is submitted in partial fulfillment of the requirements  
for the degree of

### **Master of Science**

Author: Steven J. Stine

This Thesis has been read and approved by the Examining Committee:

---

Dr. Christopher Goyne, Advisor

---

Dr. Chloe Dedic, Advisor

---

Dr. Thomas Ward, Committee Chair

Accepted for the School of Engineering and Applied Science:

---

Jennifer L. West, Dean, School of Engineering and Applied Science

May 2025

## Abstract

This study investigates the impacts of a nanosecond, repetitively-pulsed discharge on optical emission and pressure measurements in an ethylene-fueled, dual-mode scramjet combustor. The experiments were performed in the University of Virginia Supersonic Combustion Facility (UVASCF). High frame rate (50-100 kHz) spectrally filtered imaging, optical emission spectroscopy, and high frequency pressure measurements were synchronously acquired to assess the improvements induced by the discharge-coupled cavity compared to nominal fuel-lean and low-temperature cavity flameholding operation. Increased production of relevant excited-state hydrocarbon combustion radicals ( $\text{OH}^*$ ,  $\text{CH}^*$ , and  $\text{C}_2^*$ ) was observed during discharge actuation across all test cases in both spectrally filtered images and emission spectra. Spatial distribution of increased emission varied for each combustion radical. The impacts of the discharge were observed to depend on local fuel availability and were enhanced at lower stagnation temperatures. Spatial and modal analyses revealed that the discharge instigated forward shifts and an increase in width of the reaction zone for all interrogated intermediate species. Assessment of  $\text{CH}^*$  temporal dynamics in the cavity and cavity shear layer showed that nanosecond discharge actuation increased  $\text{CH}^*$  production throughout the shear layer with a maximum increase observed at  $3.5 \mu\text{s}$  from peak discharge emission. This study presents new findings on dual-mode scramjet flameholding enhancements provided by nanosecond discharges through observation of hydrocarbon combustion radical production on relevant timescales for plasma-enhanced combustion.

## **Funding and Disclaimers**

Effort sponsored by the U.S. Government under Other Transaction number HQ0034229CA03 between PSAH and the Government. The U.S. Government is authorized to reproduce and distribute reprints for Governmental purposes notwithstanding any copyright notation thereon. The views and conclusions contained herein are those of the author and should not be interpreted as necessarily representing the official policies or endorsements, either expressed or implied, of the U.S. Government.

This work was funded by the University Consortium for Applied Hypersonics under the Joint Hypersonics Transition Office (JHTO) with Michael King as Technical Manager. Thank you to Michael King for his support as Technical Manager throughout this program.

## Acknowledgments

I am fortunate to say that my life as a student researcher at UVA has been enriched by many amazing people. First and foremost, I would like to thank my advisors, Dr. Chris Goyne and Dr. Chloe Dedic. Thank you for fostering my curiosities, challenging me, providing support, and continuously putting your faith in me, even when I did not have faith in myself. Thank you also to Dr. Bob Rockwell, whose support in facilitating experiments and numerous pieces of engineering advice have had a profound impact on my path through grad school.

Much gratitude is owed to my friends and lab mates at the UVA Aerospace Research Lab for making the day-to-day life of a grad student more enjoyable. Being surrounded by a group of like-minded and hardworking people has been a blessing. Special thanks to Max Chern, Andrew Metro, Andrew Wanchek, and Tristan Witz, not only for your willingness to lend a hand when I needed it most, but more importantly for all the conversations, laughter, and for your friendship.

I have also had the privilege of working with and learning from experts in this field. Thank you to Alec Houpt, Isaac Kramer, and Felipe Gomez for sharing their technical expertise and providing support during experiments at UVA. Additional thanks to Tim Ombrello, Aaron Auslender, and Stephen D'Alessio for imparting invaluable technical advice that has positively impacted my development and excited me about a future in this field.

I would not be the person I am today without my family. Thank you to my parents, John and Karen, for your unwavering love and support through this process and throughout my life. You have been a constant source of encouragement and have always driven me towards doing what I am most passionate about: for this, I will always be grateful. Thank you also to my sister, Clara, for being an incredible role model of work ethic and kindness to me all these years.

Finally, thank you to my partner, Jenna, for sticking with me through it all. Whether you were right by my side or thousands of miles away, your endless patience and reassurance have gotten me through even the most challenging times. This was all made possible because of you. I promise you that I will continue to do my best to support you and your dreams in our life together, just as you have supported me.

## Contents

<b>List of Figures</b>	<b>vii</b>
<b>List of Tables</b>	<b>viii</b>
<b>1. Introduction</b>	<b>1</b>
<b>2. Experimental Methods</b>	<b>7</b>
2.1. University of Virginia Supersonic Combustion Facility . . . . .	7
2.2. Discharge Generation . . . . .	11
2.3. Data Acquisition . . . . .	11
2.4. High-speed Filtered Imaging . . . . .	12
2.5. Optical Emission Spectroscopy . . . . .	14
<b>3. Results</b>	<b>17</b>
3.1. Discharge Characterization . . . . .	17
3.2. Fuel-lean Flameholding Enhancements . . . . .	19
3.3. Spatial and Temporal Species Evolution . . . . .	26
<b>4. Conclusion</b>	<b>31</b>
<b>Appendix A: Pressure Measurements</b>	<b>39</b>
<b>Appendix B: Proper Orthogonal Decomposition</b>	<b>42</b>
<b>Appendix C: Temporal Variation of Discharge Flameholding Enhancements</b>	<b>47</b>
<b>Appendix D: Fuel-lean Blow-off Extension</b>	<b>50</b>
<b>Appendix E: Ignition via Pulsed Nanosecond Discharge</b>	<b>54</b>

## List of Figures

1	Relevant physical processes in a ns discharge-coupled dual-mode cavity flameholder with upstream fuel injection. . . . .	3
2	Schematic of test facility and optical collection areas. . . . .	9
3	Cavity flameholder detail with plasma module assembly installed. . . . .	11
4	Schematic of optical diagnostic hardware used in the current experiments, including the high-speed filtered imaging system, the OES setup, and a photodiode. . . . .	12
5	OES spectra collected at two different (x,y) locations with Case 2 flow conditions during discharge actuation. "Discharge" spectra were outside of the CSL-stabilized flame while "CSL Flame" spectra were collected far from the discharge. The elliptical collection area was 1.10 mm <sup>2</sup> for both cases. . . . .	15
6	Axial oscillation of the discharge filament length. RMS filament length, determined by subtracting the downstream and upstream-most filament intensity pixel locations, was found to be 4.16 mm. The filament was imaged in the presence of fuel at $\phi = 0.3$ with the C <sub>2</sub> * filter. . . . .	18
7	Probability distribution function of filament leading and trailing edge anchoring locations. The bimodal downstream probability distribution indicates that the filament anchoring location is affected by locally oscillatory conditions in the primary recirculation zone. . . . .	18
8	Heat map of maximum filament cavity penetration locations with each filter during Case 1. A coordinate of (0,0) mm corresponds to the cavity leading edge. Filament penetration increases slightly with global equivalence ratio but remains isolated from the typical CSL flame stabilization location. The high voltage electrode is centered at (x,y) = (25.3, -10.3) mm. Counts are plotted on a log scale. . . . .	20
9	Case 1, 100 kHz chemiluminescence, without discharge. (Top) average images; (bottom) standard deviation images. Image sets that utilized different filters were taken at different intensifier gains. . . . .	21
10	Case 1, 100 kHz chemiluminescence, with discharge. (Top) average images; (bottom) subtracted average images (flame with discharge minus flame only). . . . .	22
11	Case 2, 100 kHz chemiluminescence, with discharge. (Top) average images; (bottom) subtracted average images (flame with discharge minus flame only). . . . .	23
12	Case 3, 100 kHz chemiluminescence, with discharge. (Top) average images; (bottom) subtracted average images (flame with discharge minus flame only). . . . .	24
13	Isolines of CH* and C <sub>2</sub> * emission intensity across Cases 1, 2, and 3. For Cases 1 and 2, blue hues represent 10% of the maximum measured intensity. For Case 3, blue hues represent 20% of the maximum measured intensity. All red isolines represent a 50% intensity threshold. . . . .	24
14	Measured emission spectra across Cases 1, 2, and 3. (Top) full spectra; (bottom) spectra focused on OH*, CH*, and C <sub>2</sub> * bands. An increase in emission of flame-dominant species is evident for each band during discharge operation. . . . .	25
15	Cases 2 and 3 normalized wall pressure. Ns discharge actuation (dotted lines) showed minimal effects on combustor pressure. . . . .	26

16	Case 4, 50 kHz CH* chemiluminescence subtracted average images at different intensifier gate delays. Each average image was subtracted from an average CH* image of the flame. . . . .	28
17	First 3 POD modes of 100 kHz chemiluminescence without discharge actuation corresponding to Case 1. (Top) mode 1; (middle) mode 2; (bottom) mode 3. . . . .	30
18	First 3 POD modes of 100 kHz chemiluminescence with discharge actuation corresponding to Case 1. (Top) mode 1; (middle) mode 2; (bottom) mode 3. . . . .	31
19	Calculated theoretical dynamic response of the high frequency pressure measurement system with $L_t = 0.5$ m of Teflon tubing between the test section and the transducer. . . . .	41
20	Calculated theoretical dynamic response of the high frequency pressure measurement system with $L_t = 1.0$ m of Teflon tubing between the test section and the transducer. . . . .	41
21	Top ten singular values of each POD analysis for Case 1. . . . .	44
22	First 3 POD modes of 100 kHz chemiluminescence with and without discharge actuation corresponding to Case 2. (Top) mode 1; (middle) mode 2; (bottom) mode 3. . . . .	45
23	First 3 POD modes of 100 kHz chemiluminescence with and without discharge actuation corresponding to Case 3. (Top) mode 1; (middle) mode 2; (bottom) mode 3. . . . .	46
24	Case 4, difference between normalized 50 kHz CH* chemiluminescence without a discharge and with a discharge inspected at different intensifier gate delays. Each average image was subtracted from an average CH* image of the flame. An intensifier gate delay of 0 ns corresponds to the nominal delay from peak discharge emission, which was assigned to be 3.04 $\mu$ s. . . . .	48
25	Timing diagram depicting gate delays for each test case. Cases 1, 2, and 3 operated the discharge and high-speed imaging system at 100 kHz (10 $\mu$ s inter-pulse time), while Case 4 operated the discharge and high-speed imaging system at 50 kHz (20 $\mu$ s inter-pulse time). Nominal delay from peak discharge emission was 3.04 $\mu$ s. . . . .	48
26	Ethylene mass flow rate during a LBO test case. . . . .	50
27	Signal flow diagram of hardware activation and data acquisition triggers. . . . .	51
28	Normalized pressure near the onset of a LBO event without discharge actuation. Pressure is normalized by the average facility nozzle exit pressure. Each line represents a different x/H location of measurement during the same test case. An x/H location of 6.82, just downstream of the cavity closeout, had the largest rate of change in pressure among all transducer locations. . . . .	52
29	Subtracted average (with discharge - without discharge) contour plots of 1 kHz pressure measurements over time downstream of the cavity leading edge. (Left) discharge actuation before LBO onset; (right) discharge actuation after LBO onset. Pressures were normalized by the average facility nozzle exit pressure across all LBO events. Discharge actuation prior to LBO showed increased pressure retention compared to discharge actuation after LBO onset. . . . .	53

### List of Tables

1	Overview of test cases. . . . .	7
2	Center wavelength and bandwidth of bandpass filters. . . . .	13
3	List of pressure taps and normalized axial locations. . . . .	39
4	Thermodynamic (air) and measurement system properties applied to the referenced model. . . . .	40
5	Ignition success at different stagnation temperatures with an ethylene mass flow rate of 3.76 g/s (AT = successful ignition with air throttle, Yes = successful ignition, No = no ignition, “-“= not tested). . . . .	54

## 1. Introduction

The pursuit of developing efficient ramjet and scramjet engines for air-breathing supersonic and hypersonic flight has long been accompanied by component and system-level challenges that are driven by physical processes. Dual-mode scramjet engines provide continuous operation capabilities over a larger range of Mach numbers by bridging the ramjet to scramjet transition [1]. Dual-mode operation is characterized by the existence of a pre-combustion shock train in the scramjet isolator that introduces an adverse pressure gradient strong enough to reduce the captured flow Mach number to subsonic speeds [1, 2]. This mode of operation is also commonly accompanied by development of a thermally-choked throat that reintroduces a supersonic core flow in the presence of sufficient area relief downstream of the combustor [2]. Theoretically, dual-mode scramjet engines introduce benefits by improving specific impulse compared to rocket engines within the atmosphere [3, 4]. Despite this, these systems face multiple practical barriers that are amplified by the requirement of maintaining operability over a range of altitudes and flight Mach numbers. One of the most prominent challenges related to this constraint is sustaining combustion in increasingly high-speed flows that provide an unfavorable environment for fuel and oxidizer mixing, ignition, and continuous flameholding. Solutions enabling increased fuel-air residence times, or reduced ignition delay times, are critical to meeting flameholding requirements while also maintaining reasonable efficiency.

The fundamental limitations for flameholding in dual-mode environments are dependent on many engine and freestream flow properties [1, 2, 5–7]. The Damköhler number [5, 8], a useful dimensionless parameter for defining flameholding limits, is defined as

$$Da = \frac{\text{flow residence time}}{\text{chemical reaction time}} = \frac{L}{t_c u}, \quad (1)$$

where  $L$  is a characteristic length,  $u$  is the flow velocity, and  $t_c$  is a characteristic time. This expression can be simplified:

$$Da_{ign} = \frac{t_{res}}{t_{ign}}, \quad (2)$$

where  $t_{\text{res}}$  is the residence time of a fuel-air mixture in the engine and  $t_{\text{ign}}$  is the characteristic ignition delay time of the reactant mixture. The Damköhler number illustrates the difficulty of maintaining a stable flame during high speed flight: for a fixed-geometry dual-mode combustor and fuel choice, as flight Mach number increases,  $t_{\text{res}}$  decreases with marginal changes in  $t_{\text{ign}}$ . A Damköhler number less than 1 indicates an environment in which flameholding cannot be sustained. Typical Mach numbers associated with dual-mode and supersonic combustion environments with hydrocarbon fuels often yield Damköhler numbers close to 1, which reinforces the need for flameholding stabilization enhancements in high-speed airbreathing engines [8].

Numerous methods of creating a more favorable environment for ignition and flameholding in high-speed flows exist. From Equation (2), two primary pathways for improving flameholding are increasing the fuel-air residence time within the engine or decreasing ignition delay time of the fuel-air mixture. A number of geometric solutions have been implemented in dual-mode scramjet flowpaths to increase local fuel-air residence time, radical pooling, and mixing in the flameholding region, including ramp fuel injectors [9–11], strut-based fuel injectors [12–14], and recessed-wall cavity flameholders [15]. Cavity flameholders have been characterized at length in dual-mode scramjet ground tests and offer benefits of increased residence time, increased radical pooling, and enhanced mixing [16]. Variations in geometric parameters [17, 18] and fuel injection strategies [19–22] result in significant changes in flameholding characteristics and limitations. Reducing the ignition delay time of a fuel-air mixture below the fuel-air residence time becomes more challenging near scramjet takeover Mach numbers as the fuel-air residence time continues to decrease. A promising solution to the ignition delay and combustion radical production dilemma near ramjet and scramjet-takeover Mach numbers is actuation of a plasma discharge in the presence of available fuel-air mixtures within a cavity flameholder. A schematic of major flow processes involved in a discharge-coupled dual-mode cavity flameholder with a flame stabilized in the cavity shear layer (CSL) is presented in Figure 1.

Plasma discharges provide additional capabilities of reducing ignition delay times through several physical mechanisms. The dominant combustion enhancement mechanisms provided by a

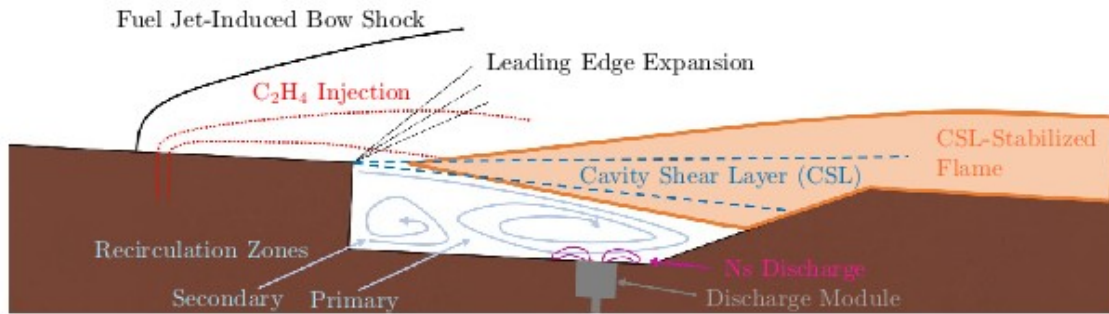


**Fig. 1:** Relevant physical processes in a ns discharge-coupled dual-mode cavity flameholder with upstream fuel injection.

plasma discharge ultimately depends on its electromagnetic characteristics, which vary with different electrode and circuit architectures, and the environment in which the discharge is actuated [8, 23, 24]. Plasma discharges are broadly divided into two categories based on the extent of equilibrium between internal energy modes of the gas within the discharge region. These energy modes can be represented as temperatures, so discharges are commonly referred to as existing in thermal equilibrium or thermal non-equilibrium states [8, 25]. Thermal equilibrium plasmas have gas temperatures similar to electronic temperatures and thermal non-equilibrium plasmas have a significantly higher electronic temperature than the local gas temperature in the discharge region. A common parameter used to distinguish discharge type and characterization of dominant species generation is through the reduced electric field strength  $E/N$ , where  $E$  is the electric field strength and  $N$  is the local gas number density [25, 26]. Plasmas with high  $E/N$  (typically greater than 50-100 Td) and electron temperatures (typically greater than about 3 eV) are dominated by reactions involving electronic activity, such as dissociation, ionization, and excitation of molecules to higher energy states resulting from direct electron impact [27]. For this reason, plasmas with large  $E/N$  are desirable for enhancing combustion through electronic and excited-state species generation that consequently accelerate chain branching reactions responsible for ignition and flame stabilization.

A number of non-equilibrium plasma discharge types have been implemented in reacting and

non-reacting environments at a wide variety of flow speeds to assess utility for combustion and flow control. Dynamics of rotational and vibrational non-equilibrium have been characterized in laminar flames coupled with pulsed microwave discharges using coherent anti-Stokes Raman scattering [28]. These pulsed discharges had an estimated  $E/N$  between 150-260 Td and resulted in noticeable increases on vibrational and rotational temperature that peaked at varying time delays. Gliding arc discharges, which typically exhibit high  $E/N$  and moderate local increases in gas temperature, have been investigated using high-speed chemiluminescence and OH planar laser-induced fluorescence (PLIF) for ignition and stabilization of laminar diffusion flames [29] and flame dynamics in scramjet combustors [30, 31]. Gliding arcs show promising results of reducing combustion mode transitions during flameholding in high-speed flows. Quasi-direct-current (Q-DC) discharges have been characterized in scramjet flowpaths in previous studies [32–36] using optical emission spectroscopy (OES), high-speed imaging, and pressure measurements, and have been shown to enable manipulation of the isolator shock train and sustain combustion at very low temperatures when co-located with a fuel jet. These plasma discharges harbor similarities in their enhancement of combustion through both thermal and non-thermal pathways, and both exhibit filamentary behavior that is heavily dependent on local flow and fueling conditions. Though these discharge types offer multiple effective mechanisms for combustion enhancement, in supersonic combustors, it is desirable to implement discharge types that have lower net power requirements.

Nanosecond repetitively-pulsed discharges typically operate with the largest  $E/N$  and electron temperatures of all known discharge types with notable reductions in required power for operation [8, 24, 25, 37]. Nanosecond discharges have been demonstrated to have excellent capabilities of enhancing combustion through generation of excited-state intermediate species and free radicals. These discharges have been characterized extensively in near-atmospheric pressure air with different electromagnetic characteristics [23, 38–41] and have been studied with diagnostics including optical emission spectroscopy, cavity ring-down spectroscopy, two-photon absorption laser-induced fluorescence (TALIF), PLIF, and high-speed imaging. Regimes of breakdown within the classification of nanosecond repetitively-pulsed discharges depend on a number of factors, most

importantly local gas composition and pressure, applied voltage, and electrode configuration and material. The extent of ignition enhancement of nanosecond discharges has also been studied in both low-speed and high-speed fuel-air mixtures. In low-speed flows, OH concentration dynamics [42–44] have been evaluated with respect to ignition success and discharge-flame interactions with optical diagnostics such as OES and PLIF. Other studies in low-speed reacting flows emphasize the importance of discharge pulse repetition frequency and pulse energy on inter-pulse coupling and hydrocarbon fuel-air mixture ignition delay times [45–47], indicating that inter-pulse coupling and ignition delay times are coupled as functions of local flow characteristics and detonation front propagation. Similar studies on ignition probability and ignition kernel propagation in the presence of a nanosecond discharge have been carried out in supersonic flows that utilize cavity flameholders [37, 48, 49]. Despite the plethora of studies that utilize these discharges for ignition and combustion enhancements, the impacts of pulsed nanosecond discharges on continuous flameholding and excited-state species generation has not yet been studied in a dual-mode environment. This distinction is critical as cavity flameholding limits differ significantly from cavity ignition limits. Analysis of steady-state flameholding across a range of stagnation enthalpies and equivalence ratios with and without actuation of a pulsed ns discharge is required to assess the impacts of such a system across a simulated flight envelope.

The overarching goal of the presented work is to examine the effects of continuously-pulsed nanosecond discharges on flameholding in a dual-mode scramjet combustor coupled with a cavity flameholder. This goal can be divided into the following objectives:

1. Characterize the oscillatory motion and spectral content of a ns discharge integrated in the base of a cavity flameholder,
2. Demonstrate that actuation of a ns repetitively-pulsed discharge in a cavity-based dual-mode scramjet test section increases simple hydrocarbon combustion radical production within a fuel-lean cavity shear layer-stabilized flame, and
3. Evaluate the impacts of a ns discharge on spatial and temporal flameholding characteristics

in a cavity-based dual-mode scramjet test section.

This paper will first outline the experimental methods, which will encompass the experimental test facility, the nanosecond discharge system, and the diagnostic hardware and imaging systems. High speed spectrally filtered imaging, optical emission spectroscopy, and wall static pressure measurements were utilized to characterize ns discharge behavior and evaluate the benefits of discharge actuation on steady state and near fuel-lean flameout dual-mode operation. The results section will be divided according to the objectives of the experiments. These objectives represent several original contributions to the topic of dual-mode flameholding and plasma-assisted flameholding at continuous timescales. Ns discharge emission oscillations in the presence of an available fuel-air mixture in a cavity flameholder have not been characterized previously with high-speed filtered imaging across all of the major hydrocarbon excited-state radical emission bands. The positive influence of a ns discharge on vital hydrocarbon excited-state species production in a cavity shear layer-stabilized flame has not been interrogated simultaneously via high-speed filtered imaging and optical emission spectroscopy prior to these experiments. The longevity of ns discharge impacts on excited-state species production within the shear layer is presented for the first time, and decomposition of the discharge-flame interactions into dominant spatial modes represents another significant contribution. Collectively, this paper advances the fundamental understanding of spatial and temporal interactions of a ns discharge with a scramjet flame, which introduces the potential for performance improvement driven by these interactions.

## 2. Experimental Methods

Definitions of the test cases in this study, and their corresponding flow and hardware parameters, are summarized in Table 1. All test cases were completed at a steady state equivalence ratio and are divided according to changes in parameters. Those available for variation included discharge pulse repetition frequency (PRF), imaging acquisition gate delay, fuel mass flow rate ( $\dot{m}_{fuel}$ ), global equivalence ratio ( $\phi$ ), facility stagnation temperature ( $T_0$ ), and facility stagnation pressure ( $P_0$ ). Case 1 explores excited-state species concentration with and without a discharge present at nominal operating conditions. Case 2 investigates a different global equivalence ratio at identical facility flow conditions. Case 3 repeats Case 2 at a lower stagnation temperature to examine discharge effectiveness at lower simulated flight enthalpies. Case 4 provides insight on the temporal evolution of CH\* emission at increasing delays from the onset of the discharge.

**Table 1:** Overview of test cases.

Case	Ns PRF (kHz)	Gate Delay (ns)	$\dot{m}_{fuel}$ (g/s)	$\phi$	$T_0$ (K)	$P_0$ (kPa)
1	100	5	3.76	0.3	1200	300
2	100	5	2.51	0.2	1200	300
3	100	5	2.78	0.2	1000	300
4	50	5-3000	2.51	0.2	1200	300
Uncertainty (%)	-	-	$\pm 0.7$	$\pm 2.0$	$\pm 0.8$	$\pm 1.0$

### 2.1. University of Virginia Supersonic Combustion Facility

All experiments described in this work were performed at the University of Virginia Supersonic Combustion Facility (UVASCF), which is an electrically-heated, direct-connect combustion tunnel capable of operating at stagnation temperatures that simulate up to Mach 5 flight enthalpies. The facility nozzle is contoured to produce a Mach 2.04 inflow to the test section. The nominal operating air mass flow rate of the facility is  $185 \pm 3.1$  g/s. To compare the effects of a ns discharge on flame stability across the dual-mode operational envelope, some test cases at a reduced stagnation temperature were conducted. These test cases maintained nominal stagnation pressure because of

operational constraints, which resulted in an increase of the air mass flow rate to a maximum of 203 g/s for a stagnation temperature of 1000 K. Global equivalence ratio was matched to compare test cases at different stagnation temperatures, so an increase in fuel mass flow rate was required to achieve the same global equivalence ratio at lower stagnation temperatures.

Figure 2 depicts a schematic of UVASCF with details on optical collection areas. A detailed explanation of the optical diagnostic setup can be found in Sections 2.4. and 2.5. Instrumentation and major flowpath features are referenced by the ratio of the distance to the leading edge of the cavity flameholder to the depth of the cavity ( $1 x/H = 9.04$  mm). The test section begins with the isolator, which is a straight-walled component with a width of 38.1 mm, a height of 25.4 mm, and a length of 485 mm. A 2.9-degree divergence begins 53.3 mm upstream of the cavity leading edge. The cavity flameholder is formed by a 9.04 mm step perpendicular to the diverging wall and a base parallel to the flow that extends 31 mm downstream of the leading edge. The cavity terminates 53.3 mm downstream of the leading edge after a 22.5-degree closeout ramp. The 2.9-degree divergence continues until the end of the combustor section 146 mm downstream of the leading edge. Optical access is provided in this section via two-9.53 mm-thick fused silica windows. The constant area section is crucial for the development of a thermal throat across a range of global equivalence ratios, which produces a pre-combustion shock train that is characteristic of dual-mode combustion. The constant area section terminates 286 mm downstream of the cavity leading edge. The diverging section begins at this location with a 2.9-degree expansion. Injection of compressed air can occur at 339 mm downstream of the cavity leading edge if additional backpressure is desired. This is commonly used for ignition of the flowpath at nominal conditions by injection of hydrogen. The end of the diverging section marks the end of the test section, where the flow exhausts to atmospheric pressure conditions 1.04 m downstream of the isolator entrance.

To enable integration of a plasma module into the flowpath, a new cavity flameholder was fabricated for the UVASCF test section. This cavity flameholder was designed with identical internal geometry to the cavity flameholder used in Ref. [21], but alteration of instrumentation location was required to enable plasma module integration. Plasma modules were located 25.3 mm upstream

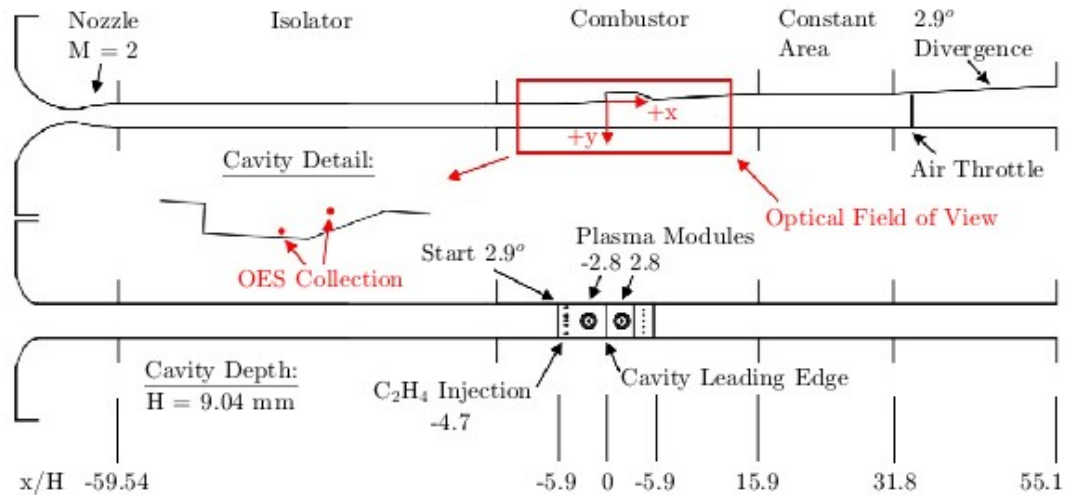


**Fig. 2:** Schematic of test facility and optical collection areas.

and 25.3 mm downstream of the cavity leading edge. The location of the downstream plasma module was selected to investigate the effects of the ns discharge on flameholding when implemented in an environment near the mean location of the flame stabilized in the cavity shear layer (CSL). The location of the upstream plasma module was selected for its proximity to the fuel supply to study effects of the ns discharge on relatively fuel-rich local fuel-air mixtures. Initial experiments at UVASCF showed that the upstream plasma module had less of an effect on emission intensity in the CSL than the downstream plasma module, so all results presented in this study will focus on the downstream plasma module location.

Five sonic, 1.25 mm diameter injection orifices located 43.2 mm upstream of the cavity leading edge supplied gaseous ethylene fuel to the test section. The transverse locations of these ports were symmetric about the axial centerline with an offset of 0 mm, 5.1 mm, and 14.2 mm from the centerline in the transverse direction. The uneven spacing was a result of alterations to the active cooling channel locations that were required due to mechanical constraints imposed by the plasma modules. Mass flow controllers (Alicat CODA Coriolis) were used to control the mass flow rate supplied through these injector ports. The mass flow controllers were operated remotely through

a microcontroller (Raspberry Pi 4) to enhance input-output capabilities. The axial and transverse locations of the ethylene injectors are labeled in proximity to the plasma modules in Figure 2. An orifice located 2.5 mm downstream of the cavity leading edge was used to supply hydrogen to the cavity for ignition without the ns discharge.

The test section was instrumented with a combination of high frequency and low frequency pressure transducers that were installed at axial locations between the isolator entrance and the atmospheric exhaust. The location and frequency of axial static wall pressure measurements can be found in Table 3 in Appendix A. To collect high frequency measurements, pressure transducers (Omega model PX309,  $\pm 0.25\%$  accuracy) were connected to the test section via a short length (0.5-1 m) of Teflon tubing that was compression bound to a 50 mm-long stainless steel tube with a small spring. The response time of the high frequency transducers when mounted directly to the desired measurement plane is  $< 1$  ms, but the dynamic response of the high frequency pressure measurement system also depends primarily on the length of Teflon tubing between the transducers and the test section. Using a theoretical model that has been validated with experimental results for single transducer volume measuring systems [50, 51], the maximum response time for this system was found to be between 4.3 and 6.7 ms (see Appendix A). This extended response time does not significantly impact the observed trends in high frequency pressure measurements during discharge actuation. Analog voltages were converted to a corresponding pressure through a real-time measurement unit (dSpace MLBX 1302T) at a sampling rate of 1 kHz. Low frequency measurements were collected at a rate of 50 Hz using a National Instruments NetScanner interface chassis (model 98RK-1) with five-16 channel scanner modules (model 9816,  $\pm 0.05\%$  accuracy) that interfaced with the test section in a similar way to the high frequency transducers. Wall temperature measurements made with type K thermocouple probes (Omega) helped to monitor the thermal state of the flowpath. Duplicate  $x/H$  transducer locations represent symmetric transverse offsets from the axial centerline that were required due to alteration in the cavity cooling structure. This offset is 14.2 mm in all cases.

## 2.2. Discharge Generation

All ns discharges in this study were generated using a custom flush-mounted plasma module with a co-annular plane-to-plane electrode configuration. Figure 3 details the installation of the plasma module in the cavity base. The electrode assembly consists of a cylindrical tungsten rod, which acts as the high voltage electrode, that is surrounded by a layer of alumina ceramic for insulation. A custom high voltage power supply (Magna) and pulse generator (Transient Plasma Systems) coupled with the plasma module assembly supplied 10 ns full-width at half-maximum (FWHM), 18 kV peak voltage pulses. Average plasma power was 450 W for discharge pulse repetition frequencies (PRF) of 50 kHz and 900 W for a PRF of 100 kHz. Ns discharges exhibited filamentary behavior and produced a short filament between the high voltage electrode and the copper wall of the combustor, which acted as an electrical ground. Characterization of filament behavior within the cavity will be discussed in Section 3.1.

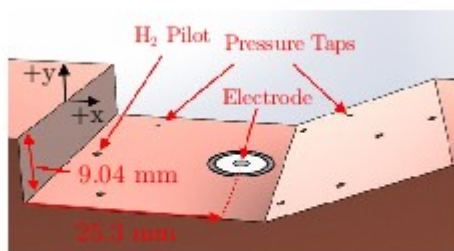
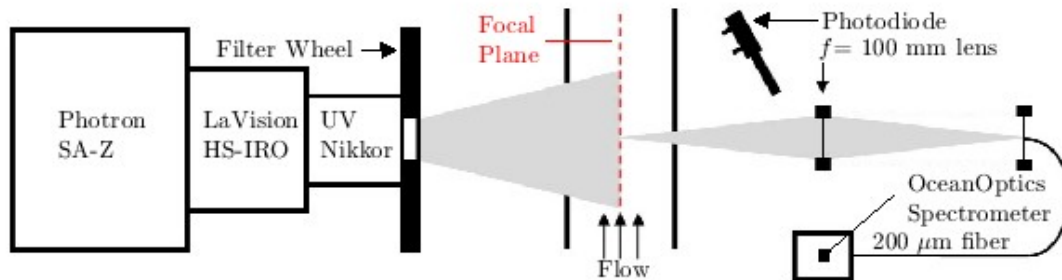


Fig. 3: Cavity flameholder detail with plasma module assembly installed.

## 2.3. Data Acquisition

Multiple measurement techniques were utilized in this study to resolve various spectral and acoustic characteristics of a CSL-stabilized flame with and without presence of a discharge. A schematic of the optical setup is displayed in Figure 4. The high-speed filtered imaging setup is outlined in Section 2.4. These measurements enabled time-resolved exploration of the physical and modal structures of excited-state species emission within the flame in relation to important

flowpath features. A photodiode was utilized to monitor total emission intensity in the combustor. This ensured safe operation of the high-speed imaging hardware (mitigated overexposure from high-intensity discharge emission) and was used to verify delay of discharge filament generation relative to the timing pulse responsible for triggering discharge generation. The optical emission spectroscopy (OES) setup, which provided more precise spectral information than achievable with the high-speed filtered imaging setup, is covered in Section 2.5.



**Fig. 4:** Schematic of optical diagnostic hardware used in the current experiments, including the high-speed filtered imaging system, the OES setup, and a photodiode.

## 2.4. High-speed Filtered Imaging

The high-speed filtered imaging configuration in this experiment utilized a Photron Fastcam (model SA-Z) high-speed CMOS camera coupled with a high-speed UV-sensitive intensifier (LaVision HS-IRO) to acquire filtered images. Bandpass filters for selective visualization of OH\* (Edmund Optics 67-280), CH\* (Edmund Optics 65-137), and C<sub>2</sub>\* (Edmund Optics 65-154) were mounted in a motorized filter wheel (Edmund Optics 84-889), which enabled fast transitions across different test cases. Table 2 lists the center wavelength and FWHM of each filter with the associated intensifier gain setting corresponding to each wavelength region of interest.

The high-speed intensifier provided capabilities of assigning precise gate delays (as low as 5 ns), which enabled the inspection of emission intensity at precisely set delays from the onset of a ns discharge. The ns discharge itself emitted light multiple orders of magnitude more intense than the

**Table 2:** Center wavelength and bandwidth of bandpass filters.

Emission Band	Center Wavelength (nm)	FWHM (nm)	Intensifier Gain (%)
OH(A-X)	$313 \pm 3$	$10 \pm 2$	45
CH(A-X)	$430 \pm 2$	$10 \pm 2$	35
C <sub>2</sub> (d-a)	$520 \pm 2$	$10 \pm 2$	40

flame at peak intensity. Two actions were taken to ensure safe operation of the intensifier during discharge actuation. The first was restriction of the intensifier gate width to 5  $\mu$ s for all test cases, which both reduced the chance of overexposure and enabled sufficient intensifier phosphor screen offloading ( $< 3 \mu$ s decay time to 1%) at an acquisition rate up to 100 kHz. This gate width provided adequate flame signal for each emission band of interest. The second safeguard was an additional 3.04  $\mu$ s delay from peak discharge intensity set based on the output voltage of the photodiode during discharge operation. All average high-speed spectrally filtered images presented here were subtracted by an average background image. In Cases 1-4, the pulsed ns discharge operated at the designated frequency for one second. The high-speed imaging system acquired images for 100 ms at a frequency equal to the ns discharge frequency in each test case.

The field of view of this imaging system, which is represented in red in Figure 2, was 544 pixels in height by 256 pixels in width with an absolute pixel resolution of 192  $\mu$ m. This field of view enabled visualization of the ns discharge, the CSL-stabilized flame, and discharge-flame interactions relative to critical flowpath features. It extended axially from downstream of the ethylene injectors ( $x/H = -3.29$ ) to downstream of the cavity closeout ramp ( $x/H = 8.11$ ) and transversely from below the base of the cavity to the top flowpath wall.

Eigenvalue decomposition methods, specifically those rooted in the singular value decomposition (SVD), offer significant benefits in analysis of critical data set features. Proper orthogonal decomposition (POD) and dynamic mode decomposition (DMD) have been employed previously in analysis and design efforts across a wide variety of disciplines, including turbulent fluid flow modal analysis [52, 53], optimal sensor placement and model reduction [54–56], and supersonic combustion mode identification [31, 57, 58]. Application of POD to high-speed filtered image data

can provide an enhanced understanding of fluctuations in spatial intensity distribution of certain spectral emission bands of interest within the flameholding region. A more detailed description of the POD algorithm and its application to high-speed filtered images is provided in Appendix B.

## 2.5. Optical Emission Spectroscopy

All OES data was gathered using a fiber-coupled spectrometer (Ocean FX-UV-VIS) with sensitivity to wavelengths between 200-850 nm and an optical resolution of 1.5 nm. Light from the flowpath centerline was re-imaged onto a 200  $\mu\text{m}$  fiber optic cable using a 4f configuration that utilized a  $f = 100$  mm focal length lens. Light collected by the fiber was then delivered to the spectrometer. The 4f configuration was constructed with a cage assembly similar to Ref. [59]. The collection area of this system was determined to be 1.10  $\text{mm}^2$ . The size and position of the collection areas are shown relative to the cavity flameholder above in Figure 2.

Spectral content collected by the OES system varied with increasing distance from the discharge. Initial OES data collection at different (x,y) locations guided selection of an acquisition location relative to the discharge for the current study. Average spectra collected at the discharge and CSL flame locations shown in Figure 2 are plotted in Figure 5. Emission intensity was normalized by the peak emission between both spectra. Near-discharge data at (x,y) = (23.4, -7.1) mm was taken at a PRF of 10 kHz in previous experiments while CSL flame data at (x,y) = (45.2, -1.9) mm was taken in the current study at a discharge PRF of 100 kHz. Many discharge-generated spectral emission bands that have been studied in both atmospheric pressure air and mixed fuel-air ns discharge environments [33, 35, 38, 41] appear in the near-discharge collection case. Discharge generated emission such as the NO  $\beta$ ,  $\gamma$ , and  $\delta$  bands, the O<sub>2</sub> Schumann-Runge band, the second positive (N<sub>2</sub> (C-B)) and first negative (N<sub>2</sub><sup>+</sup> (B-X)) nitrogen bands, and the CN (B-X) band appear near the high voltage electrode but not downstream in the CSL-stabilized flame. The CSL flame location was used for all collected spectra in the current study because of the goal of investigating effects the discharge had on flameholding rather than the spectral characteristics of the discharge itself.

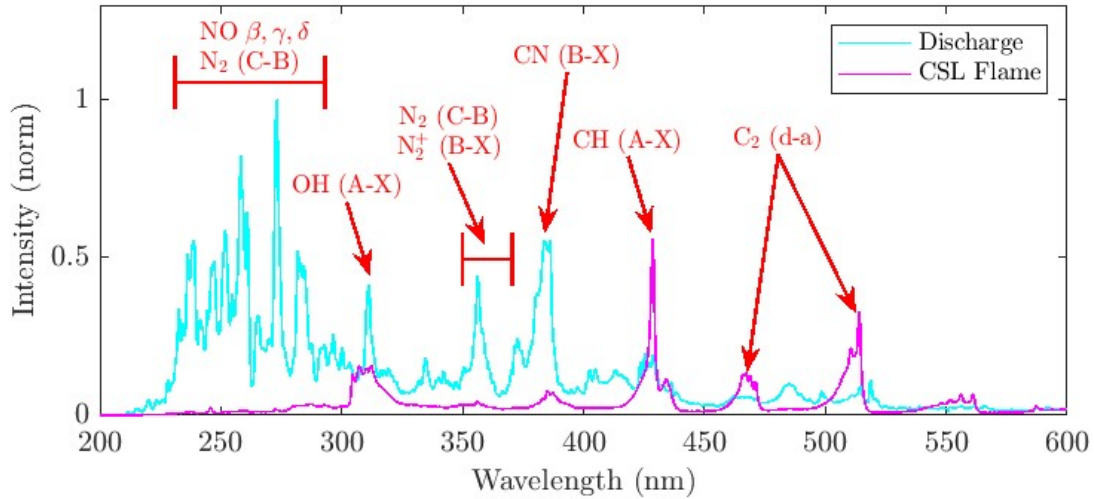


**Fig. 5:** OES spectra collected at two different (x,y) locations with Case 2 flow conditions during discharge actuation. "Discharge" spectra were outside of the CSL-stabilized flame while "CSL Flame" spectra were collected far from the discharge. The elliptical collection area was  $1.10 \text{ mm}^2$  for both cases.

Investigating the impact of the pulsed discharge on local flame behavior required precise alignment of trigger signals for facility subsystems and data collection. Nanosecond discharge generation, high-speed spectrally filtered imaging, optical emission spectroscopy, and wall static pressure measurements (50 Hz and 1 kHz) were controlled via trigger signals dependent on the test case type. Event and data collection sequences were initiated by a pulse delay generator (Berkeley Nucleonics Corp., Model 565). Three different channels generated command signals for discharge generation, high-speed imaging system exposure, and OES and pressure data acquisition, respectively. All three channels operated in burst mode. The repetition frequencies of all discharge generation and data collection events were synchronized through the internal time period of the pulse delay generator and verified using a digital oscilloscope (Tektronix Model MSO22). The discharge inter-pulse time was  $10 \mu\text{s}$  for a PRF of 100 kHz and  $20 \mu\text{s}$  for a PRF of 50 kHz, and the length of the pulse train was one second in all test cases. High-speed filtered imaging began 100 ms after the start of the test sequence to allow for the discharge system to reach steady state operation. The high-speed imaging system then acquired images for 100 ms with a nominal 3.04

$\mu\text{s}$  delay from peak discharge emission. Peak discharge emission was characterized by photodiode voltage. Additional delays up to  $6.04 \mu\text{s}$  were assigned for Case 4 tests, which examined the effects of the discharge on the flame at different delays from peak emission. Trigger pulses for all other subsystems, including high frequency pressure (1 kHz), low frequency pressure (50 Hz), and OES measurements (512 Hz), were generated by sending a trigger from the pulse delay generator to another programmable pulse delay generator (Labsmith LC880) to facilitate synchronous acquisition at lower rates.

### 3. Results

The following sections are divided according to contributions towards the objectives of this study. Discharge emission characterization will be discussed Section 3.1. Discharge impacts on CSL-stabilized flame emission intensity will be addressed in Section 3.2. The spatio-temporal characterization of these impacts will be outlined in Section 3.3. Additional discussion on temporal discharge effects is provided in Appendix C. Additional data on flameholding operability enhancements via pulsed ns discharge, including impacts on lean blow-off (LBO) and ignition, can be found in Appendix D and Appendix E.

#### 3.1. Discharge Characterization

Understanding the interaction of the discharge with the available reactant mixture in the cavity and CSL requires an understanding of filament motion within this region. Discharge filament length was calculated by iterating image columns in the +y direction over a rectangular region of interest that spanned from the cavity base to half of the cavity depth to find the furthest upstream and downstream pixels above a threshold representative of typical discharge emission intensities. A description of discharge filament length over time imaged through the  $C_2^*$  filter is shown in Figure 6. RMS filament length was found to be 4.16 mm, and frequent oscillations are observed. To better understand mechanisms for axial filament extension, a probability distribution function of upstream and downstream filament extension was constructed and is plotted in Figure 7 with the furthest upstream high intensity emission shown in red and the furthest downstream high intensity emission shown in blue. The high intensity discharge emission is most frequently bounded 1 mm upstream of and 1.8 mm downstream of the high voltage electrode. Large oscillations of the most upstream filament location are less frequent than large oscillations of the most downstream filament point, which is evident from the bimodal nature of the downstream probability distribution. This bimodal distribution, coupled with the oscillatory filament length shown in Figure 6, suggests that the downstream anchoring location of the filament is influenced by the conditions near the start of the cavity closeout ramp. Similar trends of oscillatory filament length and anchoring locations

were observed for other bands of interest.

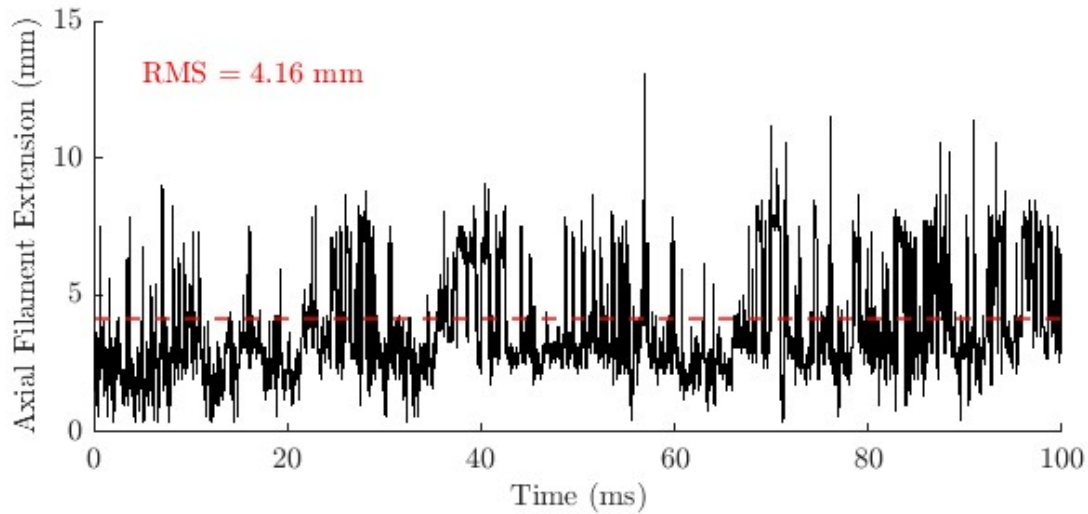


**Fig. 6:** Axial oscillation of the discharge filament length. RMS filament length, determined by subtracting the downstream and upstream-most filament intensity pixel locations, was found to be 4.16 mm. The filament was imaged in the presence of fuel at  $\phi = 0.3$  with the  $C_2^*$  filter.

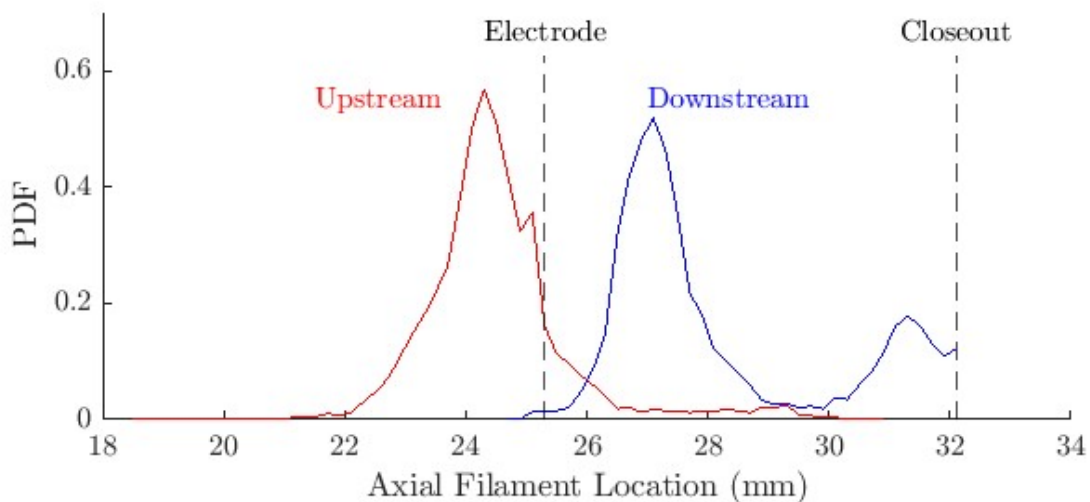


**Fig. 7:** Probability distribution function of filament leading and trailing edge anchoring locations. The bimodal downstream probability distribution indicates that the filament anchoring location is affected by locally oscillatory conditions in the primary recirculation zone.

Perhaps the most important filament behavior to detail is the depth of penetration into the cavity flameholder towards the CSL. Doing so would ensure that any observed increase in excited-

state species emission intensity can be attributed to an increased rate of combustion reactions rather than broadband emission from the discharge. Figure 8 displays heat maps of the most probable regions of maximum high-intensity emission penetration into the cavity for all filters in Case 1 conditions. These heat maps were generated using the same region of interest as Figures 6 and 7 but instead iterating image rows in the  $-x$  direction from the top edge to the bottom edge. Counts in this figure are plotted on a log scale. The first important result from these plots is that the high intensity discharge emission is most frequently anchored close to the cavity base. This region never extends into the typical CSL-stabilized flame region with infrequent extension to  $y = -5.6$  mm or less for all interrogated bands. Each of these plots also recovers the bimodal nature of the filament extension for each band of interest, with a significant number of maximum penetration depths occurring both just ahead of the high voltage electrode at an  $x$ -location of 25.3 mm (greater than 1000 occurrences) as well as closer to the start of the cavity closeout ramp (100's to 1000 occurrences). It is important to recognize that the discussion of axial and transverse filament motion in the previous paragraphs pertain to a gate delay of  $3.04 \mu\text{s}$  and that the behavior of the filament at peak intensity has not been characterized in this configuration. All of these observations provide confirmation that differences in excited-state species production in the CSL-stabilized flame that arise during discharge actuation can be attributed to combustion reactions rather than broadband discharge emission in this configuration. Effects of discharge filament spatial distribution on spatial and temporal flameholding characteristics is reported in Section 3.3.

### 3.2. Fuel-lean Flameholding Enhancements

Identification of flameholding characteristics with and without a discharge present at nominal flow conditions provides an initial comparison the effects of the discharge on radical production in the flame stabilization region. Figure 9 depicts average and standard deviation filtered images using each of the filters listed in Table 2 for Case 1 without discharge actuation. Intensities of  $\text{OH}^*$ ,  $\text{CH}^*$ , and  $\text{C}_2^*$  are highest in the CSL as evident from the average images.  $\text{OH}^*$  intensity and fluctuations in intensity are more prevalent in the CSL and less prevalent in proximity to the

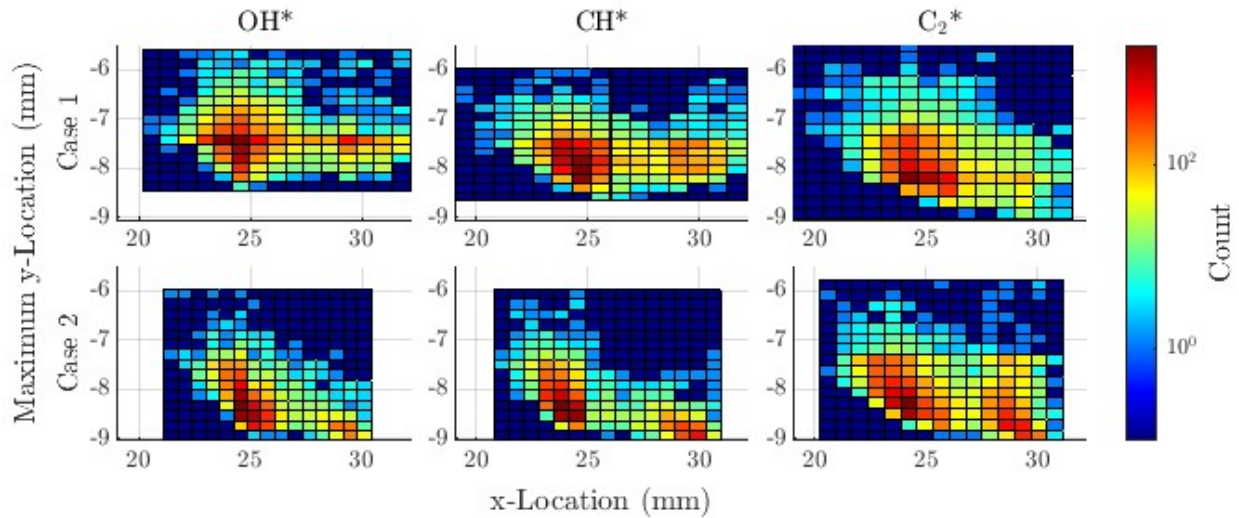


**Fig. 8:** Heat map of maximum filament cavity penetration locations with each filter during Case 1. A coordinate of (0,0) mm corresponds to the cavity leading edge. Filament penetration increases slightly with global equivalence ratio but remains isolated from the typical CSL flame stabilization location. The high voltage electrode is centered at  $(x,y) = (25.3, -10.3)$  mm. Counts are plotted on a log scale.

closeout ramp.  $C_2^*$  exhibits fluctuations in intensity that are concentrated more heavily in the shear layer and near the cavity closeout ramp than downstream of the cavity.  $CH^*$  intensity fluctuations, similar to  $OH^*$ , are significant within the shear layer and extend downstream of the cavity. Fueling above the lean limit of approximately  $\phi = 0.14$  in this UVASCF configuration produces a flame that remains anchored in the CSL. Infrequent combustion stabilization mode shifts into the fuel jet wake upstream of the cavity leading edge occur and increase in frequency as equivalence ratio increases. At or below  $\phi = 0.3$ , stabilization in the shear layer is dominant.

Direct comparison of filtered images with and without a ns discharge reveals intermediate species emission intensity and distribution are both affected in the presence of a discharge in the base of the cavity flameholder. Figure 10 depicts  $OH^*$ ,  $CH^*$ , and  $C_2^*$  filtered images corresponding to Case 1 with discharge actuation. The top row contains average images while the bottom row represents the difference of discharge on and off images at equivalent flow conditions. The intensity of each excited-state reactant increases in the presence of the discharge, but the distribution of this increased intensity varies. Differences in  $OH^*$  and  $CH^*$  intensity are most notable in the CSL,

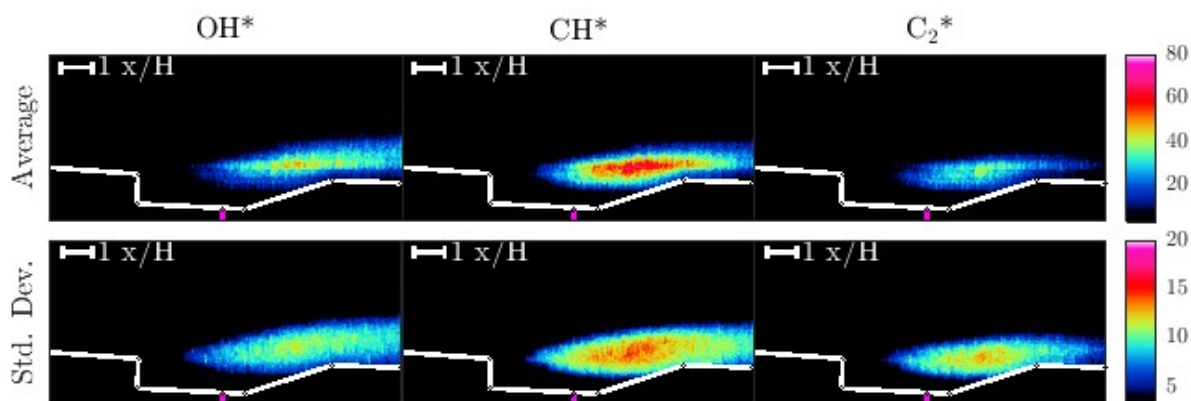


**Fig. 9:** Case 1, 100 kHz chemiluminescence, without discharge. (Top) average images; (bottom) standard deviation images. Image sets that utilized different filters were taken at different intensifier gains.

and both represent a forward shift in anchoring location and an increase in width of the reaction zone. The effect of the discharge on  $C_2^*$  production is visibly further downstream, including downstream of the cavity closeout ramp. This influence was also noticeable on the anchoring point. All three subtracted average images indicate an increased emission intensity in the CSL and a flame that is being stabilized deeper into the cavity. For the remainder of the high-speed imaging results presented here,  $OH^*$  will be omitted due to its similarity in spatial distribution of intensity changes to  $CH^*$  and its larger region of spectral overlap with plasma-dominant excited-state species than  $CH^*$  [33, 35].

Understanding the impacts of a ns discharge on fuel-lean flameholding requires additional classification at lower equivalence ratios closer to the fuel-lean flameholding limits. Figure 11 displays a similar series of filtered images to Figure 10 but corresponds to Case 2. In each case, the effects of the discharge on intensity are less significant in Case 2 compared to Case 1. Differences also exist in spatial species distribution from the higher global equivalence ratio. Increased  $CH^*$  intensity compared to the flame-only condition is localized near the cavity closeout ramp as compared to the forward portion of the reaction zone in the higher equivalence ratio case. The overall affected area of each intermediate excited-state reactant is reduced at the lower global equivalence

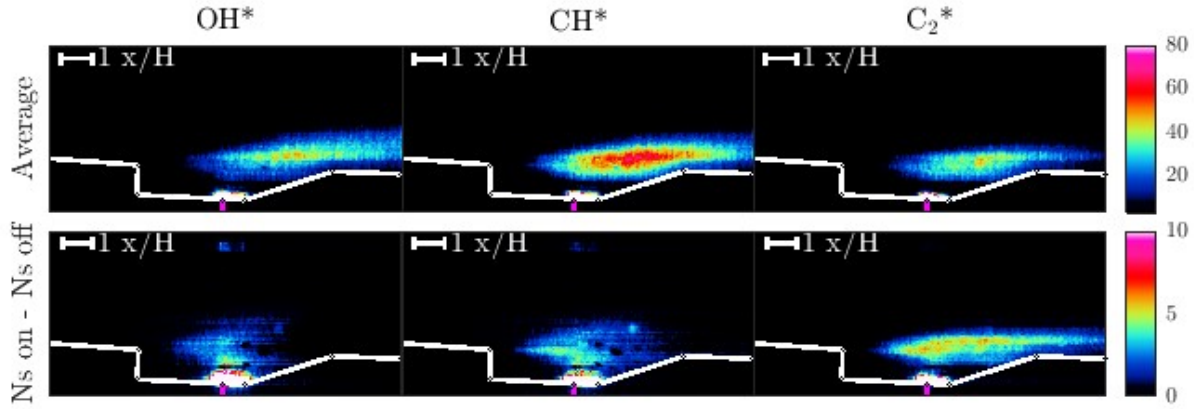


**Fig. 10:** Case 1, 100 kHz chemiluminescence, with discharge. (Top) average images; (bottom) subtracted average images (flame with discharge minus flame only).

ratio. The affected perimeter outside of the discharge broadband emission region, which is visible in pink and white at the base of the cavity in the subtracted average images, also appears to decrease compared to the higher equivalence ratio case. From this, it is evident that the effects of local equivalence ratio in the cavity has an impact on increased reactivity provided by the discharge. Comparisons of the region of intense emission that surround the discharge in Figures 10 and 11, as well as the distribution of transverse filament extension in Figure 8, also indicate that higher local equivalence ratios result in increased filament elongation in the transverse direction. The localization of enhanced  $\text{CH}^*$  emission near the cavity closeout ramp is influenced by the extension of the filament in the axial direction and therefore enhanced interaction with fuel entrained in the primary recirculation zone. Increased  $\text{C}_2^*$  emission is observed to occur in the center of the CSL but was found to be less prominent compared to the increased emission observed at a higher equivalence ratio.

Case 3, which corresponds to the same global equivalence ratio but a lower  $T_0$  than Case 2, further explores the impact of local equivalence ratio on discharge effectiveness. The series of images corresponding to Case 3 in Figure 12 show an increased reaction zone width compared to a discharge off case under the same conditions for both  $\text{CH}^*$  and  $\text{C}_2^*$ . In both average and subtracted average images, a change in discharge-flame interaction and flame anchoring is observed. Two

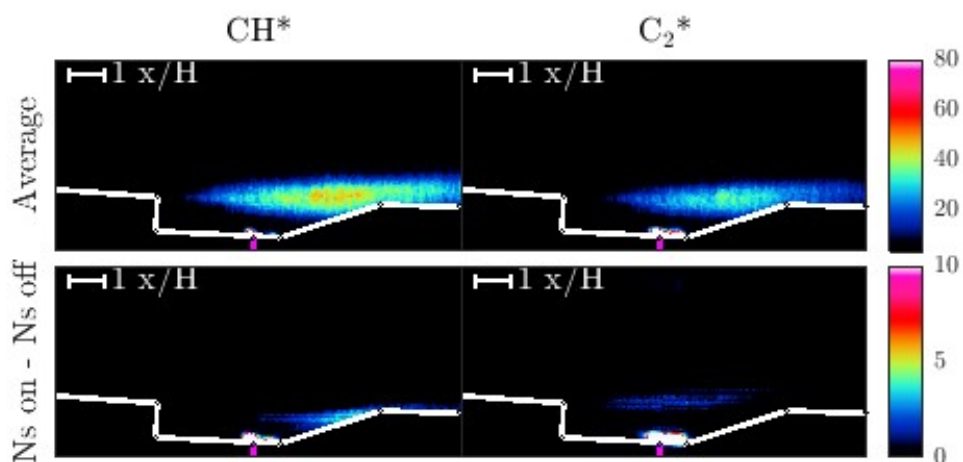


**Fig. 11:** Case 2, 100 kHz chemiluminescence, with discharge. (Top) average images; (bottom) subtracted average images (flame with discharge minus flame only).

important conclusions can be drawn from Case 3. The first is that the ns discharge was found to have a greater relative impact on flame anchoring and excited-state species production at lower  $T_0$ . This trend is made clear by comparing the high global equivalence ratio images (Case 1) with the low global equivalence ratio images at lower  $T_0$  (Case 3). The relative intensity difference from discharge on versus discharge off for  $\text{CH}^*$  and  $\text{C}_2^*$  is similar between the two cases despite Case 3 operating with both a lower global equivalence ratio and a lower total fuel flow rate. The second finding is that discharge effectiveness on flameholding is significantly impacted by local equivalence ratio and fuel entrainment. This is evident in comparing the low equivalence ratios of Case 2 and Case 3: despite the stagnation temperature difference, the observed intensity difference is greater in Case 3 in the presence of a higher fuel flow rate than Case 2.

Isocontours that portray a summary of discharge effects on  $\text{CH}^*$  and  $\text{C}_2^*$  distribution are presented in Figure 13 for Cases 1-3. Pale solid lines represent cases with a discharge while opaque dashed lines represent cases without a discharge. All red colors represent a relative 50% maximum flame intensity threshold while blue colors represent a 10% threshold for Cases 1 and 2 and a 20% threshold Case 3. These isolines confirm the critical trends observed in Figures 10-12. With ample fuel availability in the CSL and recirculating in the cavity, the discharge has an effect on excited-state species production presenting as a forward shift in flame anchoring, an increase in reaction

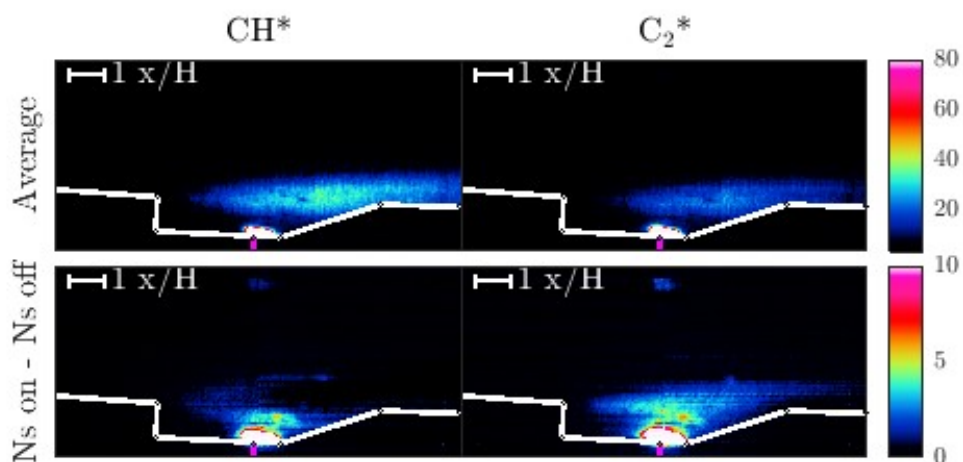


**Fig. 12:** Case 3, 100 kHz chemiluminescence, with discharge. (Top) average images; (bottom) subtracted average images (flame with discharge minus flame only).

zone width, and an increase in emission intensity in the center of the shear layer. The effects are more prevalent at higher fuel flow rates and at lower temperatures.

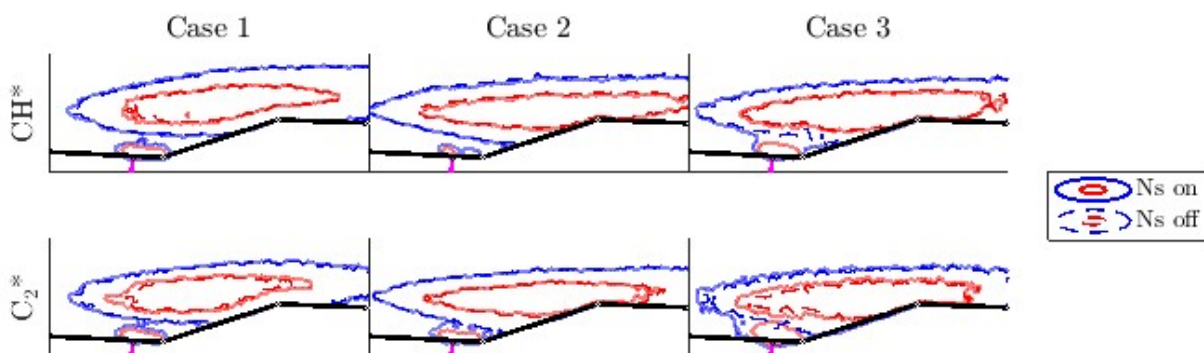


**Fig. 13:** Isolines of  $\text{CH}^*$  and  $\text{C}_2^*$  emission intensity across Cases 1, 2, and 3. For Cases 1 and 2, blue hues represent 10% of the maximum measured intensity. For Case 3, blue hues represent 20% of the maximum measured intensity. All red isolines represent a 50% intensity threshold.

Collection of more precise spectral content was completed using the OES setup during Cases 1, 2, and 3. Spectra gathered across these test cases are displayed in Figure 14. Each data set was averaged over 60 scans, background subtracted, and normalized by the maximum  $\text{CH}^*$  peak across all test cases. An increase in emission intensity near the cavity closeout ramp is observed for  $\text{OH}^*$ ,

CH\*, and C<sub>2</sub>\* with the fiber-coupled spectrometer in all spectra corresponding to Cases 1 and 2. Increased emission is observed in all relevant bands in Case 3 but is most significant in the OH\* band. These relationships corroborate the trends visualized with the high-speed filtered images given the collection area provided in Figure 2. It should also be noted that discharge-dominant species are not visible in any case with the discharge. Discharge actuation did increase emission of the CN(B-X) band in the CSL; this band, however, typically appears outside of the discharge filament and in the flameholding region with this discharge configuration.

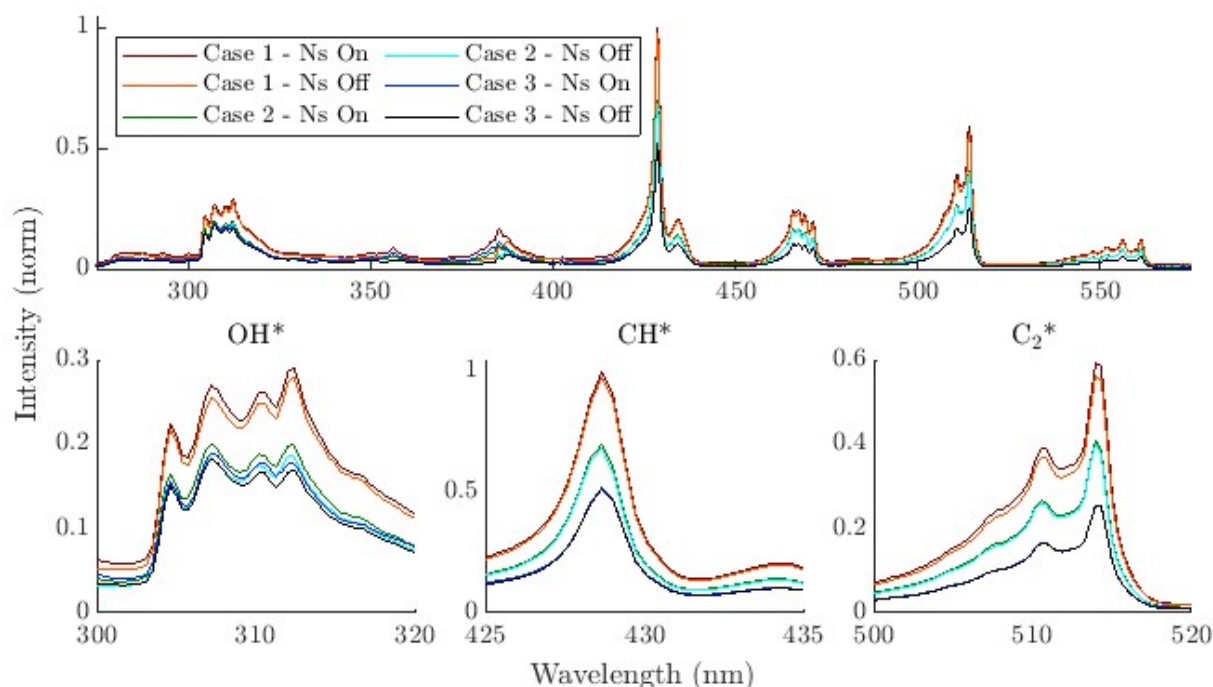


**Fig. 14:** Measured emission spectra across Cases 1, 2, and 3. (Top) full spectra; (bottom) spectra focused on OH\*, CH\*, and C<sub>2</sub>\* bands. An increase in emission of flame-dominant species is evident for each band during discharge operation.

The influence of ns discharges on combustor pressure is also of interest for dual-mode engine development. Figure 15 plots averaged wall pressure measurements normalized by the facility nozzle exit pressure at each  $T_0$  for  $\phi = 0.2$ . Each data set combines low and high frequency measurements that were acquired synchronously. Solid lines represent flameholding conditions during discharge actuation, while flame-only conditions are represented by dashed lines. Across all test

cases, for a given stagnation temperature, there were no significant impacts of the cavity discharge on combustor pressure. An increase in combustor pressure is observed over a facility stagnation temperature decrease while  $\phi$  is held constant during Case 3. The shock train leading edge location can be estimated visually with the sharp increase in normalized wall pressure upstream of the cavity leading edge. Both low temperature conditions result in a shock train leading edge position that is slightly further upstream than the high temperature conditions. This is a result of decreasing the ratio of stagnation temperatures before and after heat release due to combustion, which in turn increases the pressure upstream of the heat release.

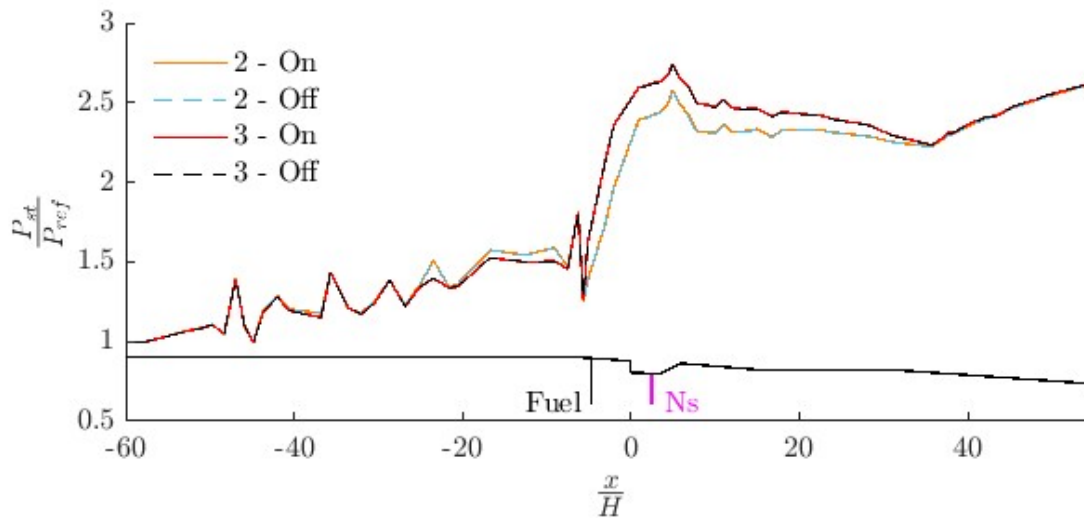


**Fig. 15:** Cases 2 and 3 normalized wall pressure. Ns discharge actuation (dotted lines) showed minimal effects on combustor pressure.

### 3.3. Spatial and Temporal Species Evolution

Previous discussions of ns discharge effects on CSL-stabilized flameholding have been restricted to minimized intensifier gate delays that provided safe exposure conditions. Examining flame emission intensity at different time delays from the ns discharge would offer insight on the longevity and spatial development of the improved radical species production. Figure 16 displays a series of average  $\text{CH}^*$  chemiluminescence images corresponding to Case 4. The images in Figure 16 were processed by subtracting the average image corresponding to each intensifier gate delay

from the flame only average image at the same conditions. From this series of images, a time history of discharge effects on the CSL-stabilized flame is developed. It is important to note that each of the intensifier gate delays listed here is an additional delay from the nominal gate delay in other test cases, which was set to  $3.04 \mu\text{s}$  after the time at which the peak discharge emission occurred. At additional delays of 50 and 100 ns, the increased intensity is located within the CSL flame region nearest the discharge filament, indicating that the discharge provides the CSL with additional excited state CH radicals. This supply of radicals is far from the high intensity filament yet is still coupled with the filament. By 250 ns, a region of increased intensity propagates along the combustor wall downstream towards the closeout ramp and the start of the divergence while remaining anchored to the discharge region. For the next 250 ns, this region moves upstream and into the center of the CSL. At further increased gate delays, the region of increased intensity once again propagates downstream but continues to decrease in magnitude for the rest of the sampled gate delays. Additional gate delays of 5.04 and 6.04  $\mu\text{s}$  were omitted but showed little effects similar to a 4.54  $\mu\text{s}$  gate delay. The increase in CH\* emission in the shear layer from time delays between 3.29 - 4.04  $\mu\text{s}$  after peak discharge emission shows that the discharge provides a stream of electronically excited radicals that increases CSL stabilized flame intensity over a large spatial region.

Improvements in excited state radical production can also be investigated by examining shot-to-shot spatial fluctuations in chemiluminescence intensity. Comparisons of contributions to dual-mode flameholding spatial modes between discharge on and off cases were made for Cases 1-3 by employing POD on the time series filtered images. POD analyses were executed with a  $72 \text{ mm} \times 26.9 \text{ mm}$  region of interest that encompassed primary regions of flame oscillations in the CSL to reduce required computation. An intensity threshold was applied to generate a mask for the ns discharge region. This mitigated saturation of the dominant spatial modes by the high intensity emission near the high voltage electrode and focused the spatial mode results on the CSL flameholding impacts. The lowest-order spatial POD modes from filtered chemiluminescence data contribute most significantly to overall spatial fluctuation of excited-state species emission in the

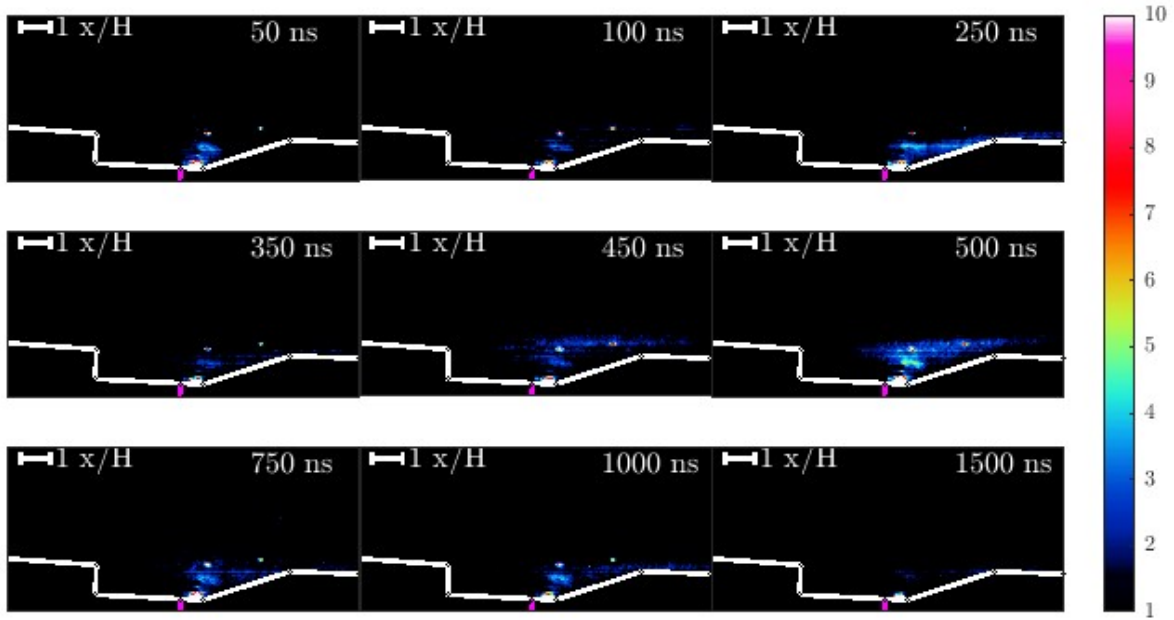


**Fig. 16:** Case 4, 50 kHz CH\* chemiluminescence subtracted average images at different intensifier gate delays. Each average image was subtracted from an average CH\* image of the flame.

flameholding region. Each presented POD mode was normalized independently of the other modes and reconstructed into a representative image scaled identically to other modes. Red and blue regions represent spatial correlations and anti-correlations [53] of chemiluminescence intensity in the flameholding region. Regardless of phase, colors near either end of the scale represent regions of larger amplitude oscillations of a given spatial POD mode.

The three lowest-order spatial POD modes for Case 1 are illustrated in Figures 17 and 18 for each of the intermediate species of interest with no discharge actuation and with discharge actuation, respectively. Rows denote flameholding spatial mode shapes while columns indicate excited-state intermediate species. The lowest-order mode for each combustion radical without discharge actuation closely resembles the expected flame shape seen in Figure 9, indicating that production of OH\*, CH\*, and C<sub>2</sub>\* is dominant in the CSL but varies significantly in amplitude throughout this region across the acquisition window. The second spatial POD mode reveals a pattern that is similar for each of the excited-state intermediate species: oscillations occur from the freestream

side of the CSL to the cavity closeout side of the flame stabilization region. For each of the first two mode shapes in Figure 17 (from left to right), a reduction in protrusion of significant oscillations into the freestream is evident. Mode 3 shows a significant upstream to downstream oscillation perpendicular to the freestream for OH\*. The third mode shapes for CH\* and C<sub>2</sub>\*, however, indicate that these oscillations in chemiluminescence intensities are more significantly impacted by the presence of the primary recirculation zone [19] and its interaction with the CSL. Analyses of the three lowest order spatial modes detail important interactions between the freestream, CSL, and cavity recirculation regions that influence oscillations in chemiluminescence intensity for various intermediate species.

Construction of spatial POD modes during discharge actuation provides a method for assessing changes in intensity oscillations for each of the radical species of interest compared to cases without discharge actuation. Figure 18 displays the same spatial POD modes as Figure 17 with discharge actuation. For each of the intermediate species of interest, zones of intensity fluctuations observed in the lowest order mode are pulled slightly upstream and towards the base of the cavity. In each case, the production of excited-state species in the CSL is correlated with the production of excited-state species closer to the base of the cavity and the electrode. The most significant change in spatial distribution of intensity fluctuations is observed in mode 3 for all intermediate species. Comparing Figure 18 with Figure 17, regions of oscillation associated with exchange of excited-state species between the primary recirculation region and the CSL are pulled upstream and into the cavity flameholder more significantly during discharge actuation. Regions of OH\* intensity fluctuations represent the largest change of the three intermediate species for mode 3, displaying a shift from CSL-freestream exchange to cavity recirculation-CSL exchange with increased penetration into the freestream near the same axial location as the discharge. This change is also observed for the other two excited-state radicals in mode 3, but is less significant than the observed change for OH\*. Similar to mode 1, discharge actuation is correlated with these changes in spatial distribution of intensity fluctuations. The singular values corresponding to the top ten spatial POD modes of Case 1 are provided in Appendix B. Aside from the lowest order mode for C<sub>2</sub>\*, discharge opera-

tion had minimal effects on total chemiluminescence intensity fluctuations. Discharge operation, however, did have an observed effect on spatial distribution of the lowest order modes as shown in Figure 18. POD analysis of other conditions revealed similar trends to average filtered images targeting each excited state radical: the discharge was shown to have less of an effect on spatial flameholding modes at leaner conditions at high temperatures (Case 2) and a slightly larger effect on spatial flameholding modes at lower temperatures (Case 3). Further discussion on these trends can be found in Appendix B. Overall, at Case 1 conditions, POD analyses showed that the discharge had a significant effect on spatial distribution of intensity fluctuations, and therefore flame stabilization, within the cavity and the CSL-stabilized reaction zone. Though discharge operation had insignificant effects on axial pressure distributions, coupled results of spectrally-filtered images, OES spectra, temporal discharge and discharge-flame evolution, and POD analyses indicate that discharge actuation had positive impacts on overall flame intensity and flame stabilization during dual-mode operation.

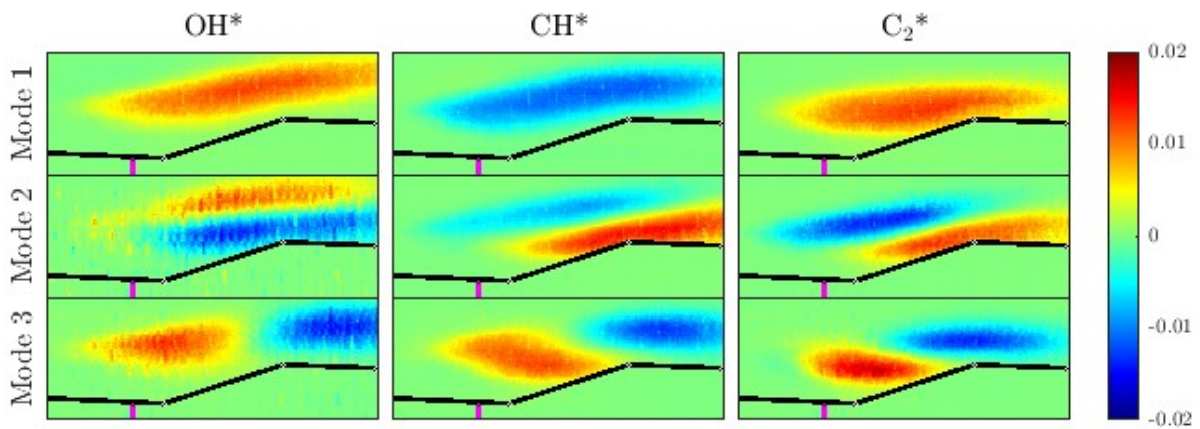


**Fig. 17:** First 3 POD modes of 100 kHz chemiluminescence without discharge actuation corresponding to Case 1. (Top) mode 1; (middle) mode 2; (bottom) mode 3.

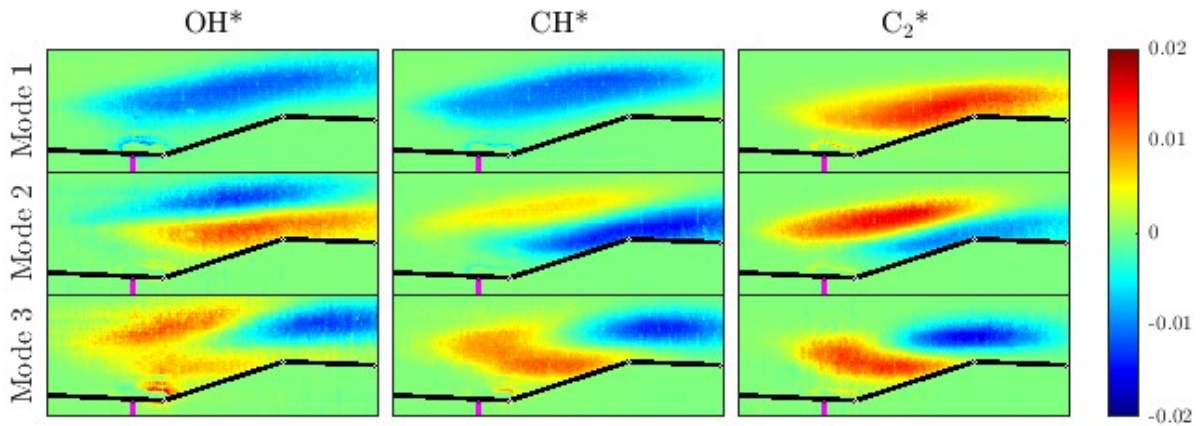


**Fig. 18:** First 3 POD modes of 100 kHz chemiluminescence with discharge actuation corresponding to Case 1. (Top) mode 1; (middle) mode 2; (bottom) mode 3.

#### 4. Conclusion

Experiments at the University of Virginia Supersonic Combustion Facility (UVASCF) examined the impacts of continuously-pulsed ns plasma discharges on dual-mode scramjet flameholding. This study aimed to characterize discharge filament behavior within the cavity flameholder, evaluate improved excited-state species production in the fuel-lean cavity shear layer-stabilized flame during discharge actuation, and explore the physical mechanisms through which the discharge impacted the flame via modal and temporal analyses. All objectives of the study were achieved here, and the major findings of this study are:

1. High speed images showed that the length and anchoring points of the ns discharge oscillated significantly over the course of a single time series and had a bimodal axial distribution near the closeout ramp. Protrusion of high-intensity emission was examined with all filters and was found to be far from the shear layer, which isolated the observed improvement in excited state radical production within the shear layer from discharge emission itself.
2. Across all test cases, enhanced production of  $\text{OH}^*$ ,  $\text{CH}^*$ , and  $\text{C}_2^*$  was observed in the cavity shear layer stabilized flame when the ns discharge was actuated. The impact of the ns discharge was found to be more profound on observed relative intensity at higher fuel flow

rates at a given temperature and at lower temperatures for the same equivalence ratio. These results indicate that ns discharges have the capability to improve flameholding over a range of dual-mode scramjet operating conditions.

3. Spatio-temporal  $\text{CH}^*$  evolution, examined through  $\text{CH}^*$  filtered imaging of steady state flameholding with a discharge, confirmed that discharge actuation influenced an increase in  $\text{CH}^*$  concentration throughout the shear layer that differs over a range of times after a ns pulse. Analysis of lowest order spatial chemiluminescence POD modes showed that the discharge forced a spatial shift in the dominant oscillations of the cavity shear layer stabilized flame. Both of these results further support the conclusion that ns discharges can provide noticeable improvements to flameholding in a fuel-lean, dual-mode scramjet.

Future investigations could further support the findings of this study. Exploration of discharge effects at stagnation temperatures as low as the low-temperature flameholding limit (about 700 K), at higher global equivalence ratios, and at different discharge PRFs would provide additional information on flameholding enhancements that could be offered over a larger range of operating conditions. Additional variation of targeted species and gate delays from peak discharge emission would further improve understanding of temporal discharge-flame interactions for other important intermediate species. The experiments presented in this paper enhance fundamental understanding of flameholding improvements via pulsed ns discharge actuation using hydrocarbon combustion radical emission as a benchmark. Variations in magnitude and distribution of increased emission intensity in the flame indicate that discharge actuation is beneficial to dual-mode flameholding over a range of operating conditions. Observed modification of spatial flameholding modes and temporal species distribution offers new fundamental knowledge that could guide selective flameholding improvements by species of interest.

## References

- [1] S. N. B. Murthy and Edward T. Curran. *Scramjet Propulsion*. AIAA Education Series. American Institute of Aeronautics and Astronautics, Inc., 2000.
- [2] Pratt D. Daley D. Heiser, W. and U. Mehta. *Hypersonic Airbreathing Propulsion*. AIAA Education Series. American Institute of Aeronautics and Astronautics, Inc., 1994.
- [3] M. Smart. Scramjets. *The Aeronautical Journal*, 111(1124):605–619, 2007. doi: 10.1017/S0001924000004796.
- [4] M. Smart. Comparison between hydrogen and methane fuels in a 3-d scramjet at mach 8. 2007.
- [5] Corin Segal. *The Scramjet Engine: Processes and Characteristics*. Cambridge Aerospace Series. Cambridge University Press, 2009.
- [6] W.H. Heiser and D.T. Pratt. Aerothermodynamics of the dual-mode combustion system. 2000.
- [7] Javier Urzay. Supersonic combustion in air-breathing propulsion systems for hypersonic flight. *Annual Review of Fluid Mechanics*, 50(1):593–627, 2018. doi: 10.1146/annurev-fluid-122316-045217.
- [8] Yiguang Ju and Wenting Sun. Plasma assisted combustion: Dynamics and chemistry. *Progress in Energy and Combustion Science*, 48:21–83, 2015. ISSN 0360-1285. doi: <https://doi.org/10.1016/j.pecs.2014.12.002>.
- [9] C. P. Goyne, C. G. Rodriguez, R. H. Krauss, J. C. McDaniel, and C. R. McClinton. Experimental and numerical study of a dual-mode scramjet combustor. *Journal of Propulsion and Power*, 22(3):481–489, 2006. doi: 10.2514/1.13215.
- [10] D. B. Le, C. P. Goyne, R. H. Krauss, and J. C. McDaniel. Experimental study of a dual-mode scramjet isolator. *Journal of Propulsion and Power*, 24(5):1050–1057, 2008. doi: 10.2514/1.32591.
- [11] R.K. Seleznev, S.T. Surzhikov, and J.S. Shang. A review of the scramjet experimental data base. *Progress in Aerospace Sciences*, 106:43–70, 2019. ISSN 0376-0421. doi: <https://doi.org/10.1016/j.paerosci.2019.02.001>.
- [12] Fabrizio Vergine, Cody Ground, and Luca Maddalena. Strut injectors for scramjets: Total pressure losses in two streamwise vortex interactions. *Journal of Propulsion and Power*, 33(5):1140–1150, 2017. doi: 10.2514/1.B36306.
- [13] D. Scherrer, Olivier Dessornes, Marc Ferrier, Axel Vincent-Randonnier, Yann Moule, V., and Sabel’Nikov. Research on supersonic combustion and scramjet combustors at onera. 2016. URL <https://api.semanticscholar.org/CorpusID:106397573>.

- [14] K.-Y. Hsu, C. D. Carter, M. R. Gruber, T. Barhorst, and S. Smith. Experimental study of cavity-strut combustion in supersonic flow. *Journal of Propulsion and Power*, 26(6):1237–1246, 2010. doi: 10.2514/1.45767.
- [15] Adela Ben-Yakar and Ronald K. Hanson. Cavity flame-holders for ignition and flame stabilization in scramjets: An overview. *Journal of Propulsion and Power*, 17(4):869–877, 2001. doi: 10.2514/2.5818.
- [16] Frank W. Barnes and Corin Segal. Cavity-based flameholding for chemically-reacting supersonic flows. *Progress in Aerospace Sciences*, 76:24–41, 2015. ISSN 0376-0421. doi: <https://doi.org/10.1016/j.paerosci.2015.04.002>.
- [17] Will O. Landsberg, Damian Curran, and Anand Veeraragavan. *Influence of Cavity Depth on Ignition and Flameholding Modes within a Scramjet Combustor*. doi: 10.2514/6.2021-4163.
- [18] Chadwick C. Rasmussen, James F. Driscoll, Kuang-Yu Hsu, Jeffrey M. Donbar, Mark R. Gruber, and Campbell D. Carter. Stability limits of cavity-stabilized flames in supersonic flow. *Proceedings of the Combustion Institute*, 30(2):2825–2833, 2005. ISSN 1540-7489. doi: <https://doi.org/10.1016/j.proci.2004.08.185>.
- [19] Steven G. Tuttle, Campbell D. Carter, and Kuang-Yu Hsu. Particle image velocimetry in a nonreacting and reacting high-speed cavity. *Journal of Propulsion and Power*, 30(3):576–591, 2014. doi: 10.2514/1.B34974.
- [20] Patton M. Allison, Kraig Frederickson, Justin W. Kirik, Robert D. Rockwell, Walter R. Lempert, and Jeffrey A. Sutton. Investigation of supersonic combustion dynamics via 50kHz ch\* chemiluminescence imaging. *Proceedings of the Combustion Institute*, 36(2):2849–2856, 2017. ISSN 1540-7489. doi: <https://doi.org/10.1016/j.proci.2016.08.039>.
- [21] Robert D. Rockwell, Christopher P. Goynes, Harsha Chelliah, James C. McDaniel, Brian E. Rice, Jack R. Edwards, Luca M. L. Cantu, Emanuela C. A. Gallo, Andrew D. Cutler, and Paul M. Danehy. Development of a premixed combustion capability for dual-mode scramjet experiments. *Journal of Propulsion and Power*, 34(2):438–448, 2018. doi: 10.2514/1.B36550.
- [22] Neta Yokev, Haim Elya Brod, Donggang Cao, and Dan Michaels. Impact of fuel injection distribution on flame holding in a cavity-stabilized scramjet. *Journal of Propulsion and Power*, 37(4):584–594, 2021. doi: 10.2514/1.B38093.
- [23] David Z. Pai, Deanna A. Lacoste, and Christophe O. Laux. Transitions between corona, glow, and spark regimes of nanosecond repetitively pulsed discharges in air at atmospheric pressure. *Journal of Applied Physics*, 107(9):093303, 05 2010. ISSN 0021-8979. doi: 10.1063/1.3309758.
- [24] S M Starikovskaia. Plasma-assisted ignition and combustion: nanosecond discharges and development of kinetic mechanisms. *Journal of Physics D: Applied Physics*, 47(35):353001, aug 2014. doi: 10.1088/0022-3727/47/35/353001.

- [25] Andrey Starikovskiy and Nickolay Aleksandrov. Plasma-assisted ignition and combustion. *Progress in Energy and Combustion Science*, 39(1):61–110, 2013. ISSN 0360-1285. doi: <https://doi.org/10.1016/j.pecs.2012.05.003>.
- [26] Yuri P. Raiizer. *Gas Discharge Physics*. Springer, 1997.
- [27] Alexander A. Fridman and Lawrence A. Kennedy. *Plasma Physics and Engineering*. CRC Press, 2011.
- [28] Chloe E. Dedic and James B. Michael. Thermalization dynamics in a pulsed microwave plasma-enhanced laminar flame. *Combustion and Flame*, 227:322–334, 2021. ISSN 0010-2180. doi: <https://doi.org/10.1016/j.combustflame.2021.01.006>.
- [29] Alexander Fridman, Alexander Gutsol, Shailesh Gangoli, Yiguang Ju, and Timothy Umbrello. Characteristics of gliding arc and its application in combustion enhancement. *Journal of Propulsion and Power*, 24(6):1216–1228, 2008. doi: 10.2514/1.24795.
- [30] Dynamic characteristics of a gliding arc plasma-assisted ignition in a cavity-based scramjet combustor. *Acta Astronautica*, 171:238–244, 2020. ISSN 0094-5765. doi: <https://doi.org/10.1016/j.actaastro.2020.03.005>.
- [31] Rong Feng, Jiajian Zhu, Zhenguo Wang, Fan Zhang, Yangyang Ban, Guoyan Zhao, Yifu Tian, Chenglong Wang, Hongbo Wang, Zun Cai, and Mingbo Sun. Suppression of combustion mode transitions in a hydrogen-fueled scramjet combustor by a multi-channel gliding arc plasma. *Combustion and Flame*, 237:111843, 2022. ISSN 0010-2180. doi: <https://doi.org/10.1016/j.combustflame.2021.111843>.
- [32] Konstantin V. Savelkin, Dmitry A. Yarantsev, Igor V. Adamovich, and Sergey B. Leonov. Ignition and flameholding in a supersonic combustor by an electrical discharge combined with a fuel injector. *Combustion and Flame*, 162(3):825–835, 2015. ISSN 0010-2180. doi: <https://doi.org/10.1016/j.combustflame.2014.08.012>.
- [33] Alexander Firsov, Konstantin V. Savelkin, Dmitry A. Yarantsev, and Sergey B. Leonov. Plasma-enhanced mixing and flameholding in supersonic flow. *Philosophical Transactions of the Royal Society A: Mathematical, Physical and Engineering Sciences*, 373(2048):20140337, 2015. doi: 10.1098/rsta.2014.0337.
- [34] Boris Leonov, Brock E. Hedlund, and Alec W. Houpt. *Morphology of a Q-DC Discharge within a Fuel Injection Jet in a Supersonic Cross-Flow*. doi: 10.2514/6.2018-1060.
- [35] Sergey Leonov, Alec Houpt, Skye Elliott, and Brock Hedlund. Ethylene ignition and flameholding by electrical discharge in supersonic combustor. *Journal of Propulsion and Power*, 34(2):499–509, 2018. doi: 10.2514/1.B36811.
- [36] Alec Houpt, Sergey Leonov, Timothy Umbrello, Campbell Carter, and Robert John Leiweke. Flow control in supersonic-cavity-based airflow by quasi-direct-current electric discharge. *AIAA Journal*, 57(7):2881–2891, 2019. doi: 10.2514/1.J058057.

- [37] Timothy M. Ombrello, Stephen D. Hammack, Campbell D. Carter, Kenneth Busby, and Joseph K. Lefkowitz. Scramjet cavity ignition using nanosecond-pulsed high-frequency discharges. *Combustion and Flame*, 262:113335, 2024. ISSN 0010-2180. doi: <https://doi.org/10.1016/j.combustflame.2024.113335>.
- [38] C O Laux, T G Spence, C H Kruger, and R N Zare. Optical diagnostics of atmospheric pressure air plasmas. *Plasma Sources Science and Technology*, 12(2):125, feb 2003. doi: 10.1088/0963-0252/12/2/301.
- [39] David Z Pai, Deanna A Lacoste, and Christophe O Laux. Nanosecond repetitively pulsed discharges in air at atmospheric pressure—the spark regime. *Plasma Sources Science and Technology*, 19(6):065015, nov 2010. doi: 10.1088/0963-0252/19/6/065015.
- [40] David Z Pai, Gabi D Stancu, Deanna A Lacoste, and Christophe O Laux. Nanosecond repetitively pulsed discharges in air at atmospheric pressure—the glow regime. *Plasma Sources Science and Technology*, 18(4):045030, oct 2009. doi: 10.1088/0963-0252/18/4/045030.
- [41] G D Stancu, F Kaddouri, D A Lacoste, and C O Laux. Atmospheric pressure plasma diagnostics by oes, crds and talif. *Journal of Physics D: Applied Physics*, 43(12):124002, mar 2010. doi: 10.1088/0022-3727/43/12/124002.
- [42] Zhiyao Yin, Igor Adamovich, and Walter Lempert. *OH Radical and Temperature Measurements During Ignition of H<sub>2</sub>-air Mixtures Excited by a Repetitively Pulsed Nanosecond Discharge*. 2012. doi: 10.2514/6.2012-826.
- [43] D L Rusterholtz, D A Lacoste, G D Stancu, D Z Pai, and C O Laux. Ultrafast heating and oxygen dissociation in atmospheric pressure air by nanosecond repetitively pulsed discharges. *Journal of Physics D: Applied Physics*, 46(46):464010, oct 2013. doi: 10.1088/0022-3727/46/46/464010.
- [44] I V Adamovich, I Choi, N Jiang, J-H Kim, S Keshav, W R Lempert, E Mintusov, M Nishihara, M Samimy, and M Uddi. Plasma assisted ignition and high-speed flow control: non-thermal and thermal effects. *Plasma Sources Science and Technology*, 18(3):034018, jul 2009. doi: 10.1088/0963-0252/18/3/034018.
- [45] Joseph K. Lefkowitz and Timothy Ombrello. An exploration of inter-pulse coupling in nanosecond pulsed high frequency discharge ignition. *Combustion and Flame*, 180:136–147, 2017. ISSN 0010-2180. doi: <https://doi.org/10.1016/j.combustflame.2017.02.032>.
- [46] Sara Lovascio, Timothy Ombrello, Jun Hayashi, Sergey Stepanyan, Da Xu, Gabi Daniel Stancu, and Christophe O. Laux. Effects of pulsation frequency and energy deposition on ignition using nanosecond repetitively pulsed discharges. *Proceedings of the Combustion Institute*, 36(3):4079–4086, 2017. ISSN 1540-7489. doi: <https://doi.org/10.1016/j.proci.2016.07.065>.
- [47] Joseph K. Lefkowitz, Stephen D. Hammack, Campbell D. Carter, and Timothy M. Ombrello. Elevated oh production from nphfd and its effect on ignition. *Proceedings of the Combustion Institute*, 38(4):6671–6678, 2021. ISSN 1540-7489. doi: <https://doi.org/10.1016/j.proci.2020.09.002>.

- [48] Stephen D. Hammack and Timothy M. Ombrello. Spatio-temporal evolution of cavity ignition in supersonic flow. *Proceedings of the Combustion Institute*, 38(3):3845–3852, 2021. ISSN 1540-7489. doi: <https://doi.org/10.1016/j.proci.2020.06.372>.
- [49] Hyungrok Do, Mark A. Cappelli, and M. Godfrey Mungal. Plasma assisted cavity flame ignition in supersonic flows. *Combustion and Flame*, 157(9):1783–1794, 2010. ISSN 0010-2180. doi: <https://doi.org/10.1016/j.combustflame.2010.03.009>.
- [50] Tjeldeman H. Bergh, H. Theoretical and experimental results for the dynamic response of pressure measuring systems by h.bergh and h.tjeldeman. 01 1965. doi: 10.13140/2.1.4790.1123.
- [51] J Kutin and A Svete. On the theory of the frequency response of gas and liquid pressure measurement systems with connecting tubes. *Measurement Science and Technology*, 29(12), nov 2018. doi: 10.1088/1361-6501/aae884.
- [52] Peter J. Schmid. Dynamic mode decomposition of numerical and experimental data. *Journal of Fluid Mechanics*, 656:5–28, 2010. doi: 10.1017/S0022112010001217.
- [53] Julien Weiss. *A Tutorial on the Proper Orthogonal Decomposition*. doi: 10.2514/6.2019-3333.
- [54] R. Semaan. Optimal sensor placement using machine learning. *Computers and Fluids*, 159: 167–176, 2017. ISSN 0045-7930. doi: <https://doi.org/10.1016/j.compfluid.2017.10.002>.
- [55] John Graff, Albert Medina, and Francis D. Lagor. Information-based sensor placement for data-driven estimation of unsteady flows. *AIAA Journal*, 61(11):4864, 2023. doi: 10.2514/1.J063015.
- [56] Andrew R. Crowell and Jack J. McNamara. Model reduction of computational aerothermodynamics for hypersonic aerothermoelasticity. *AIAA Journal*, 50(1):74–84, 2012. doi: 10.2514/1.J051094.
- [57] Yu Meng, Wenming Sun, Hongbin Gu, Fang Chen, and Ruixu Zhou. Supersonic combustion mode analysis of a cavity based scramjet. *Aerospace*, 9(12), 2022. ISSN 2226-4310. doi: 10.3390/aerospace9120826.
- [58] Shinji Nakaya, Hajime Yamana, and Mitsuhiro Tsue. Experimental investigation of ethylene/air combustion instability in a model scramjet combustor using image-based methods. *Proceedings of the Combustion Institute*, 38(3):3869–3880, 2021. ISSN 1540-7489. doi: <https://doi.org/10.1016/j.proci.2020.07.129>.
- [59] Laurie A. Elkowitz, Andrew J. Wanchek, Robert D. Rockwell, Christopher P. Goynes, Chloe E. Dedic, Qiang Le, Janett Walter-Williams, and Darrien Hunt. *Dual-Mode Scramjet Control Using Optical Emission Sensors*. doi: 10.2514/6.2023-0120.
- [60] Lawrence Sirovich. Turbulence and the dynamics of coherent structures. i - coherent structures. *Quarterly of Applied Mathematics - QUART APPL MATH*, 45, 10 1987. doi: 10.1090/qam/910463.

- [61] J. Brzozowski, P. Bunker, N. Elander, and P. Erman. Predissociation effects in the a, b, and c states of ch and the interstellar formation rate of ch via inverse predissociation. *The Astrophysical Journal*, (207):414–424, 1976. ISSN 0009-2614. doi: [https://ui.adsabs.harvard.edu/link\\_gateway/1976ApJ...207..414B/doi:10.1086/154509](https://ui.adsabs.harvard.edu/link_gateway/1976ApJ...207..414B/doi:10.1086/154509).
- [62] Peter Erman. High resolution measurements of atomic and molecular lifetimes using the high frequency deflection technique. *Physica Scripta*, 11(2):65, feb 1975. doi: 10.1088/0031-8949/11/2/001.
- [63] K.H. Becker, H.H. Brenig, and T. Tatarczyk. Lifetime measurements on electronically excited ch(a) radicals. *Chemical Physics Letters*, 71(2):242–245, 1980. ISSN 0009-2614. doi: [https://doi.org/10.1016/0009-2614\(80\)80156-4](https://doi.org/10.1016/0009-2614(80)80156-4).
- [64] N. L. Aleksandrov, S.V. Kindysheva, E.N Kukaev, S.M. Starikovskaya, and A. Yu. Starikovskii. Simulation of the ignition of a methane-air mixture by a high-voltage nanosecond discharge. *Plasma Physics Reports*, 35:867–882, 2009. doi: <https://doi.org/10.1134/S1063780X09100109>.
- [65] Andrey Starikovskiy. Physics and chemistry of plasma-assisted combustion. *Philosophical Transactions of the Royal Society A: Mathematical, Physical and Engineering Sciences*, 373: 20150074, 2015. doi: 10.1098/rsta.2015.0074.
- [66] Frédéric Grisch, Guy-Alexandre Grandin, Dominique Messina, and Brigitte Attal-Trétout. Laser-based measurements of gas-phase chemistry in non-equilibrium pulsed nanosecond discharges. *Comptes Rendus Mécanique*, 337(6):504–516, 2009. ISSN 1631-0721. doi: <https://doi.org/10.1016/j.crme.2009.06.021>.

## Appendix A: Pressure Measurements

Table 3 indicates the axial location and sampling frequencies of the static wall pressure measurements in all test cases. High frequency (1 kHz) pressure measurement locations were chosen due to proximity to the ns discharge locations and expected shock train leading edge locations relative to the cavity leading edge across a range of global equivalence ratios. The high frequency measurements taken downstream of the cavity leading edge were crucial to both LBO test sequence initiation and data collection.

**Table 3:** List of pressure taps and normalized axial locations.

Rate (Hz)	x/H	Rate (Hz)	x/H	Rate (Hz)	x/H	Rate (Hz)	x/H
1000	-58.84	1000	-23.45	1000	4.95	50	26.92
50	-57.58	50	-21.62	1000	5.74	50	28.32
50	-52.52	1000	-20.64	1000	6.82	50	29.73
50	-51.17	1000	-16.73	50	7.8	50	31.13
50	-49.71	1000	-12.58	50	8.28	50	35.69
50	-48.31	1000	-9.14	50	9.2	50	36.81
50	-46.95	50	-7.49	50	9.2	50	37.71
50	-45.86	1000	-6.26	50	10.03	50	38.22
50	-44.85	1000	-5.65	50	10.03	50	39.63
1000	-43.67	50	-5.13	1000	11.03	50	41.03
50	-41.99	1000	-3.04	50	11.03	50	42.29
1000	-40.61	50	-3.04	50	12.01	50	43.55
1000	-36.79	1000	-2.04	50	12.01	50	45.25
50	-35.67	50	-2.04	50	13.41	50	46.85
50	-33.59	1000	0.91	50	15.02	50	48.06
50	-32.01	50	0.91	50	16.74	50	49.18
1000	-30.47	1000	3.59	50	18.01	50	51.42
50	-28.64	50	3.59	50	22.71	50	51.99
50	-26.81	50	4.44	50	24.11	50	52.7
50	-25.16	1000	4.44	50	25.51	50	54.66

It is important to understand that the dynamic response of the high frequency pressure measuring system can influence synchronization of measurements with events occurring in the combustor. The response time of the transducer model used for high frequency measurements is cited as < 1 ms. This is the response time of the transducer if it was directly mounted to the test section. The additional response time required with various lengths of Teflon tubing must also be considered. A theoretical model for isentropically-expanding single transducer volume pressure measuring systems from Ref. [51] was applied at two Teflon tube lengths to calculate the dynamic response

of the combined system. Thermodynamic properties of air and dimensions of the measurement system are listed in Table 4.

**Table 4:** Thermodynamic (air) and measurement system properties applied to the referenced model.

Property	Value	Units
Density	1.204	kg m <sup>-3</sup>
Temperature	288	K
Speed of sound	340.2	m s <sup>-1</sup>
Dynamic viscosity	17.88	μPa s
Isobaric specific heat	1006	J kg <sup>-1</sup> K <sup>-1</sup>
Ratio of specific heats	1.40	-
Thermal conductivity	0.025	W m <sup>-1</sup> K <sup>-1</sup>
Teflon tube inner diameter	1.346	mm
Transducer volume	742	mm <sup>3</sup>

Figures 19 and 20 display the calculated dynamic response of the pressure measurement system at a tube length  $L_t = 0.5$  m and 1.0 m, respectively. The left column displays the amplitude ratio and phase lag of the pressure measuring system, while the right column displays the response time of the combined system. As expected, with an increased tube length, the amplitude ratio of pressure oscillations at the transducer volume to pressure oscillations at test section decreases. Resonance peaks of the amplitude response are translated to lower relative frequencies at longer tube lengths. These trends follow those presented in Refs. [50, 51] for variations in tube length. The response time of the combined system increases with tube length, with a theoretical maximum response time of approximately 6.7 ms at a tube length  $L_t = 1.0$  m compared to 4.3 ms with  $L_t = 0.5$  m. This added time delay, though important to recognize, does not represent a statistically significant response on the high frequency pressure data presented in this study as high frequency pressure measurements were taken for the entire duration of discharge actuation (1-2 s). Uncertainties in experimental thermodynamic and physical quantities also yield statistically insignificant amounts of added or reduced time delay, with an independent temperature increase to 500 K and variations of sensor volume  $\pm 400$  mm<sup>3</sup> resulting in  $\pm 1$  ms of time delay variations. In experiments with goals of fast system response and correlation of multiple instantaneous measurements, such as active control experiments, accurate characterization of thermodynamic and physical properties

that affect the response time of the pressure measuring system becomes more significant.

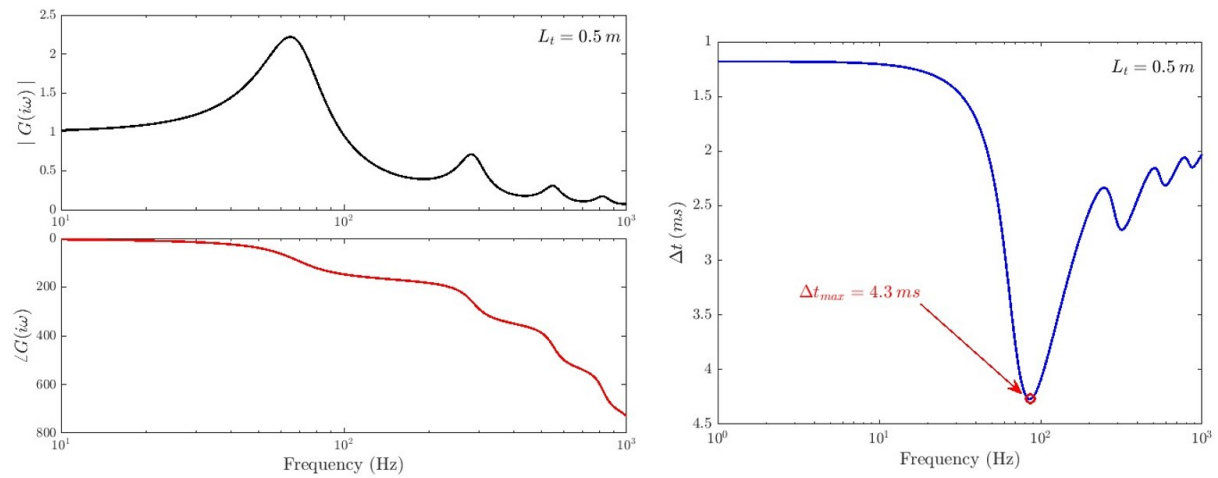


**Fig. 19:** Calculated theoretical dynamic response of the high frequency pressure measurement system with  $L_t = 0.5$  m of Teflon tubing between the test section and the transducer.

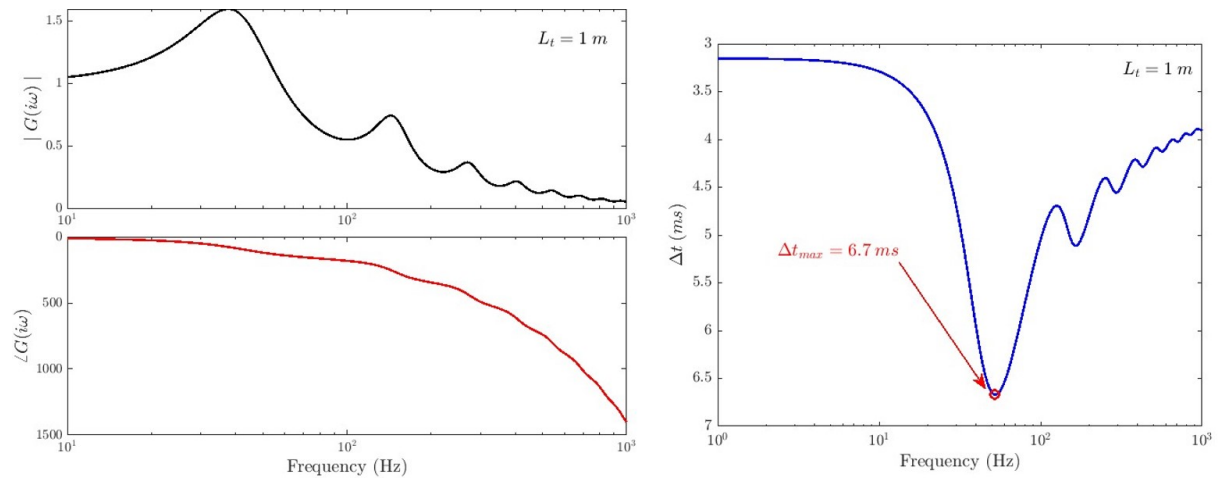


**Fig. 20:** Calculated theoretical dynamic response of the high frequency pressure measurement system with  $L_t = 1.0$  m of Teflon tubing between the test section and the transducer.

## Appendix B: Proper Orthogonal Decomposition

The POD algorithm shares many similarities with the SVD algorithm. Given the large number of pixels in the region of interest (52,500) and number of time steps (10,000) in each set of images for the current study, the method of snapshots [53, 60] was employed to reduce load of storage and computational time during post-processing. To begin, filtered images are first reshaped and arranged into 1D arrays that represent intensities of all pixels at a given timestep:

$$I_n = \begin{bmatrix} I_{(1,1)} & I_{(1,2)} & \dots & I_{(1,m)} \\ I_{(2,1)} & \ddots & & \vdots \\ \vdots & & \ddots & \vdots \\ I_{(m,1)} & \dots & \dots & I_{(m,m)} \end{bmatrix} \implies I_n = [I_1 \quad I_2 \quad \dots \quad I_{m^2}], \quad (3)$$

where  $n$  represents the  $n^{\text{th}}$  timestep and  $m$  represents a pixel index for the imaging system with a pixel resolution of  $m \times m$ . All  $n$ -1D arrays are then arranged in order to form 2D matrix that represents the entire series of high-speed filtered images:

$$I = \begin{bmatrix} I_{(1,1)} & I_{(2,1)} & \dots & I_{(n,1)} \\ I_{(1,2)} & \ddots & & \vdots \\ \vdots & & \ddots & \vdots \\ I_{(1,m^2)} & \dots & \dots & I_{(n,m^2)} \end{bmatrix}, \quad (4)$$

such that all  $n$ -1D arrays representing one timestep are arranged column-wise from beginning to end of data acquisition. The next step, which ensures that fluctuations in chemiluminescence intensity are captured, subtracts the reshaped mean chemiluminescence intensity array from each column of the 2D array in Eq. (4):

$$I' = I - I_{avg}. \quad (5)$$

Once the mean image (array) has been removed from the intensity matrix, intensity variance can

be examined through generation of a correlation matrix by normalizing the covariance intensity matrix by the number of timesteps in the dataset:

$$C_I = \frac{1}{n} I I^T. \quad (6)$$

With the correlation matrix representing intensity fluctuations across the data acquisition window, an eigenvalue problem can be solved to generate the temporal modes:

$$C_I \Phi_n = \lambda_n \Phi_{t_n} \quad (7)$$

where  $\lambda_n$  and  $\Phi_{t_n}$  represent eigenvalues and eigenvectors of the intensity correlation matrix, respectively. Here, the eigenvectors represent the temporal modes of chemiluminescence intensity fluctuations. Eigenvalues and eigenvectors are then reordered from largest to smallest eigenvalues. Sorting the eigenvalues and eigenvectors in this way allows for analysis of the dominant modes, which are the modes associated with the largest singular values and thus the modes that are most responsible for fluctuations in chemiluminescence intensity. In order to generate spatial modes, given that the method of snapshots presents a number of modes equivalent to the number of timesteps, the mean-subtracted intensity matrix is projected onto the temporal modes:

$$\Phi_s = I^T \Phi_t. \quad (8)$$

Here,  $\Phi_t$  contains all of the temporal modes and  $\Phi_s$  are the spatial coefficients, which can be normalized at each timestep to generate the spatial modes. These spatial modes are then reshaped into an image whose size matches the dimensions of the original image:

$$\Phi_s = \begin{bmatrix} \phi_{s(1,1)} \\ \phi_{s(1,2)} \\ \vdots \\ \phi_{s(1,m^2)} \end{bmatrix} \implies \Phi_s = \begin{bmatrix} \phi_{s(1,1)} & \phi_{s(2,1)} & \cdots & \phi_{s(1,m)} \\ \phi_{s(1,2)} & \ddots & & \vdots \\ \vdots & & \ddots & \vdots \\ \phi_{s(m,1)} & \cdots & \cdots & \phi_{s(m,m)} \end{bmatrix}. \quad (9)$$

Scaled images that represent spatial modes, which are arranged in decreasing order by their singular value contributions, are useful in determining which fluctuations in excited-state species production have the largest impact on flame oscillations throughout the flameholding region. These images are also useful in determining directionality of these fluctuations as the covariance of pixel intensity values is utilized to develop the correlation matrix. POD analyses of high-speed filtered image datasets with and without discharge actuation are compared in Section 3.3. Samples of calculated singular values associated with the ten lowest order modes, which represent the relative impact of a given spatial mode on overall chemiluminescence intensity fluctuations, are plotted in Figure 21 for Case 1.

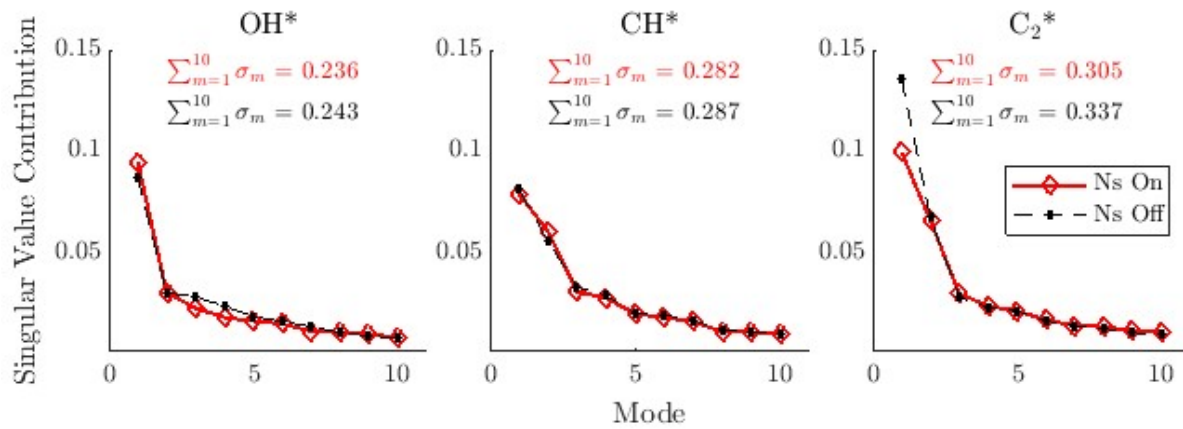


**Fig. 21:** Top ten singular values of each POD analysis for Case 1.

Much like the observed reduction of discharge effectiveness on flameholding with lower fuel availability presented in Figures 11 and 13 (Case 2), minimal differences exist between spatial distribution of intensity fluctuations with and without discharge actuation. Exploring spatial intensity fluctuations for these conditions, however, is beneficial for understanding how interactions between production of excited-state species in the cavity recirculation region and the CSL change at different fuel flow rates. A comparison of the three lowest order spatial POD modes corresponding to Case 2 with and without discharge actuation is presented in Figure 22. Notable variations in intensity fluctuations at a lower equivalence ratio include a reduction in oscillation region area and extension towards the freestream (mode 1), introduction of a larger region of anti-correlation

near the closeout ramp for  $\text{CH}^*$  (mode 1), and a splitting of correlated intensity fluctuations near the CSL in both the axial and transverse direction (mode 3). All variations from Case 1 can be attributed to the reduction of heat release from combustion in the shear layer, which, for similar cavity geometries, is accompanied by increased velocity gradients normal to the freestream flow and a lower impingement point of the CSL on the closeout ramp [19].

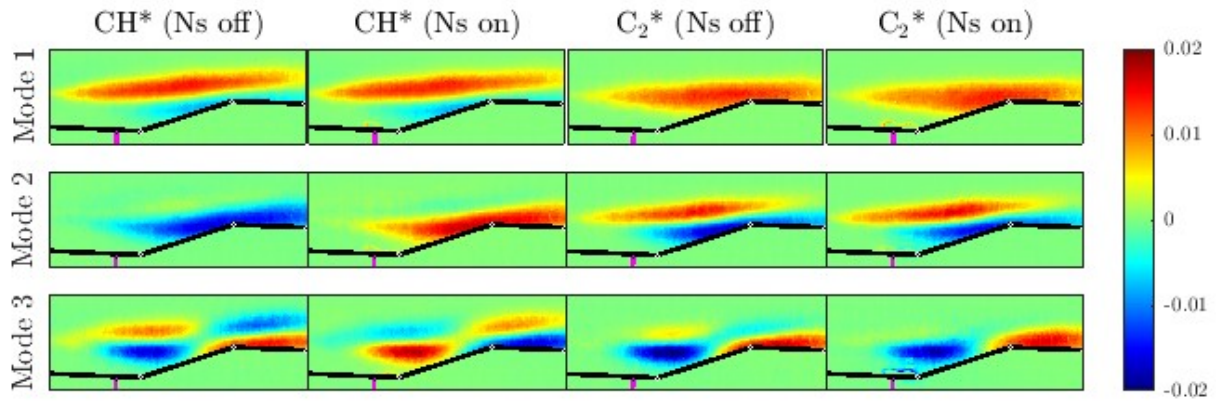


**Fig. 22:** First 3 POD modes of 100 kHz chemiluminescence with and without discharge actuation corresponding to Case 2. (Top) mode 1; (middle) mode 2; (bottom) mode 3.

Exploring spatial intensity fluctuation modes at lower temperatures provides an additional metric of comparison for discharge effects. Figure 23 shows the lowest-order POD modes during flameholding with and without discharge actuation at conditions corresponding to Case 3. Comparing the lowest order modes at a low temperature with those at the same equivalence ratios at a higher temperature shows many similarities. The most notable change between discharge on and off cases is a forward shift in  $\text{C}_2^*$  intensity fluctuations. The lowest order mode shape for both species maintains the same shape across the temperature difference, indicating that the CSL is still responsible for major intensity fluctuations at lower temperatures.

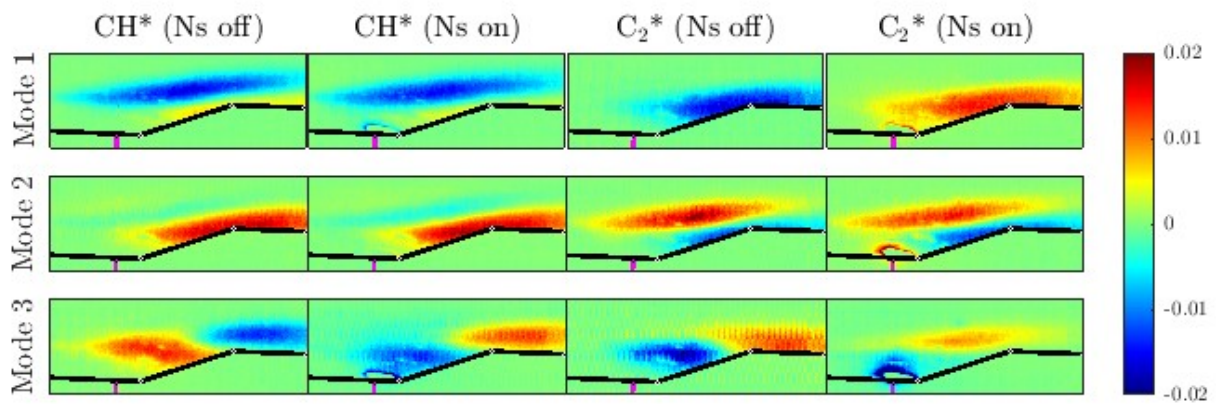


**Fig. 23:** First 3 POD modes of 100 kHz chemiluminescence with and without discharge actuation corresponding to Case 3. (Top) mode 1; (middle) mode 2; (bottom) mode 3.

## Appendix C: Temporal Variation of Discharge Flameholding Enhancements

The spatio-temporal evolution of the discharge effects on CH\* intensity in the CSL can be assessed more quantitatively by considering total counts at each case. Total contribution of the discharge to CH\* intensity in the flame, normalized by the maximum difference between discharge on and off flameholding conditions across different gate delays, is plotted in Figure 24. For each gate delay, total counts of pixels that were below a specified threshold, dictated by intensity in the discharge region, were summed and normalized by the maximum total count value across all gate delays. A significant peak exists at a delay of 500 ns from the nominal gate delay. This peak is preceded by oscillations in total intensity differences. Figure 16, as well as the subtracted CH\* image in Figure 11, show that the increase in CH\* production begins near the closeout ramp and propagates upstream and towards the freestream. The overall area of influence on CH\* intensity also increases with this shift towards a 500 ns gate delay. Two additional gate delays (2000 and 3000 ns) are included in this plot to show that after the peak intensity difference at 500 ns, the intensity difference generally decreases. Additional data points beyond a total 6.04  $\mu$ s delay from peak discharge emission would further support this conclusion. Figure 25 displays a timing diagram of gate delay variation for clarity.

The radiative lifetime of the CH(A-X) transition has been characterized at length using multiple measurement techniques. Experiments that cite the lowest uncertainties (one to three percent) have employed high frequency deflection using electron beams [61, 62] and laser induced fluorescence of inert gases [63] to measure this radiative lifetime to be between 535-545 ns. Spatial evolution of improved CH\* production displayed in Figure 16 suggested that this was due to increased availability of radicals and excited state reactants at the base of the cavity, which provided a pathway to exchange radicals with the shear layer. The directional bias of enhanced CH\* production at early delays near the closeout ramp also follows the downstream bias of the filament at a 3.045  $\mu$ s delay shown in Figure 7. As the time delay increased beyond a total 3.54  $\mu$ s, the extent of influence on emission in the shear layer continually decreases on relevant timescales to the CH(A-X) radiative lifetime. This suggests that after this time delay, increased production of excited state

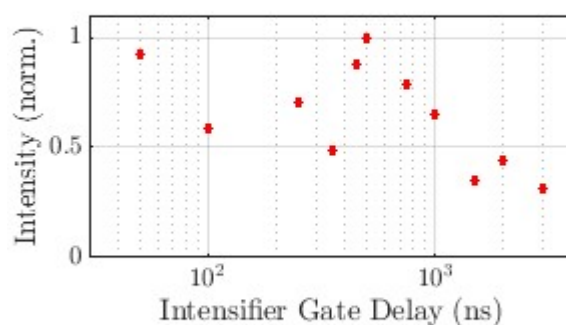


**Fig. 24:** Case 4, difference between normalized 50 kHz CH\* chemiluminescence without a discharge and with a discharge inspected at different intensifier gate delays. Each average image was subtracted from an average CH\* image of the flame. An intensifier gate delay of 0 ns corresponds to the nominal delay from peak discharge emission, which was assigned to be 3.04  $\mu$ s.

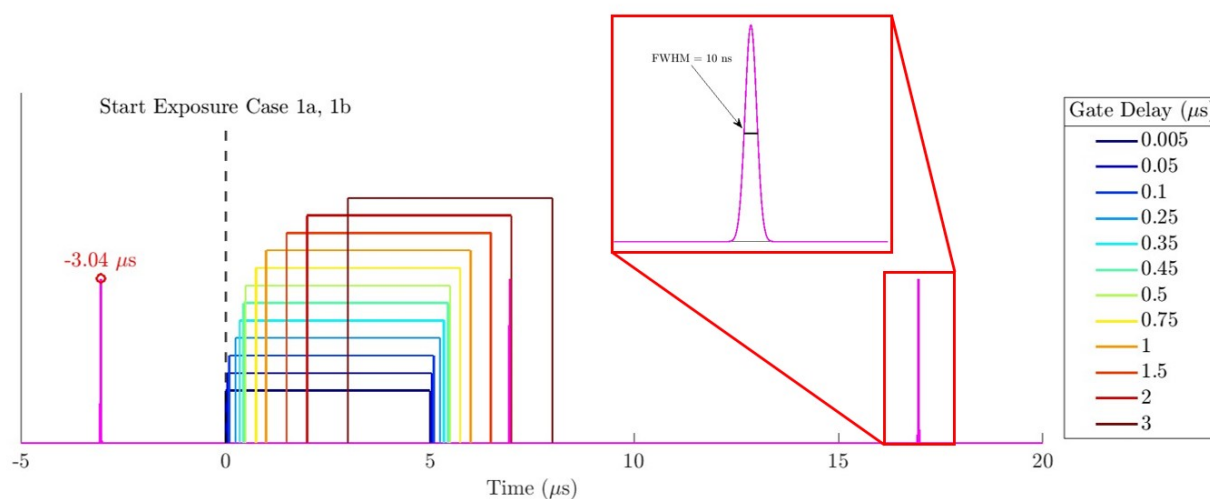


**Fig. 25:** Timing diagram depicting gate delays for each test case. Cases 1, 2, and 3 operated the discharge and high-speed imaging system at 100 kHz (10  $\mu$ s inter-pulse time), while Case 4 operated the discharge and high-speed imaging system at 50 kHz (20  $\mu$ s inter-pulse time). Nominal delay from peak discharge emission was 3.04  $\mu$ s.

radicals by the discharge is primarily decoupled from the CSL stabilized flame. The area of high intensity discharge emission also decreases over this time period and continues to decrease beyond

6  $\mu\text{s}$ , which suggests that the supply of excited state radicals to the CSL is dependent on availability of these additional species provided by the discharge filament near the cavity base. The time range from 0-3  $\mu\text{s}$ , which was not examined in filtered images in this study, has previously been experimentally assessed using OES, cavity ring-down spectroscopy, and intensified filtered imaging [41, 43]. This time range has been found to be largely dominated by elementary electronic processes such as impact excitation of  $\text{N}_2$  molecules,  $\text{O}_2$  molecules, and O atoms [8, 24, 25, 43] on the scale of  $10 < t < 1000$  ns, which proceed to collisional quenching of these excited state species to enhance O atom, fuel fragment, and radical species production on larger timescales [64, 65]. Other studies have used CH PLIF to examine temporal dynamics of the CH(C-X) band [66] and suggest that equivalence ratio plays a strong role on decay in fluorescence near a ns discharge streamer.

## Appendix D: Fuel-lean Blow-off Extension

Evaluation of LBO characteristics of cavity-based ns-discharge coupled dual-mode combustors provides potential implications on operability enhancement. Lean blow-off (LBO) test cases carried out in this study varied ethylene equivalence ratio over time during the data acquisition window. LBO tests were initialized by the start of a fuel flow rate ramp-down. This was accomplished by modifying the program used to command fuel mass flow rates to allow for a step reduction in fuel flow rate over a specified number of divisions with a set delay. A sample of a LBO fueling sequence is plotted in Figure 26. LBO test cases began with a fuel mass flow rate of  $\phi = 0.17$  and reduced fuel flow rate commands to 0 g/s at evenly spaced delays of 750 ms.

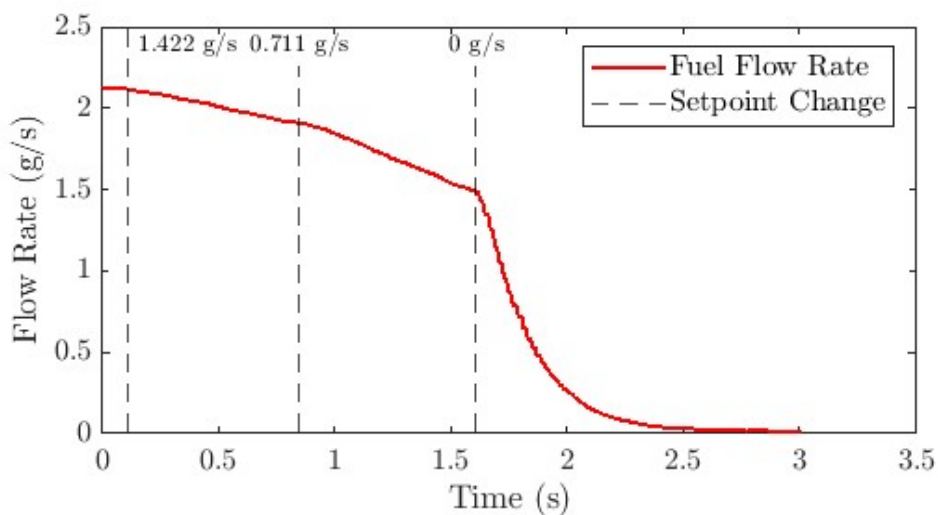


**Fig. 26:** Ethylene mass flow rate during a LBO test case.

LBO data collection triggers were identical to the baseline test cases apart from the initialization procedure. Figure 27 describes trigger signal and data acquisition sequences for both baseline (steady state  $\phi$ ) and LBO test cases. During LBO test cases, the pulse delay generator was set to be triggered externally via the real-time measurement unit according to the measured pressure near the end of the cavity closeout ramp rather than manually. Trigger pressures were assigned to explore discharge utility for near LBO flameholding and local cavity reignition following LBO onset. Once the trigger pressure was reached, a start pulse was sent from the real-time measurement unit

to the pulse delay generator. After this start pulse was received, data collection sequences were identical to baseline test cases. The ns pulse train was actuated for two seconds during LBO test cases.

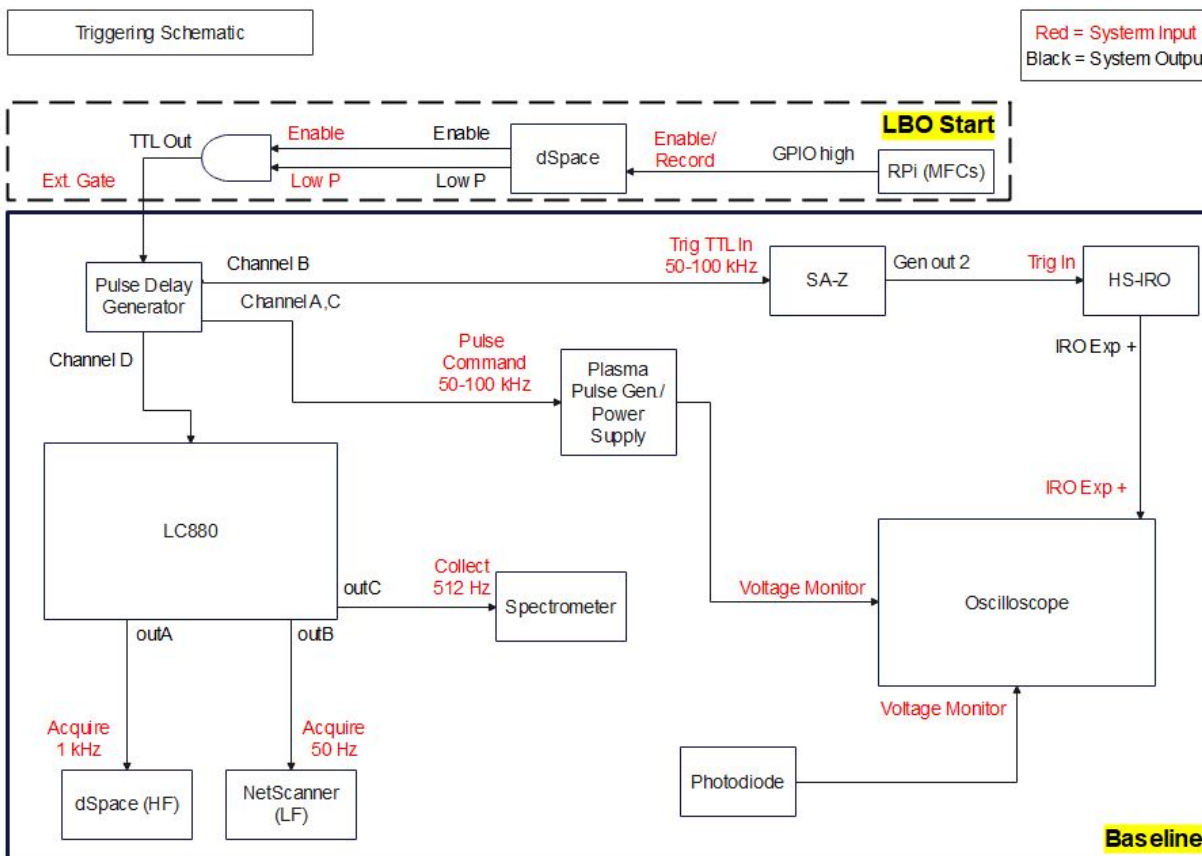


**Fig. 27:** Signal flow diagram of hardware activation and data acquisition triggers.

High-frequency pressure measurements vary significantly during LBO events according to local flowpath geometry and rate of change of global equivalence ratio. With a fixed rate of change in global equivalence ratio, sharp reductions in pressure offer a reasonable approximation of LBO time relative to the start of a test sequence. Trends in normalized pressure measurements at different  $x/H$  locations during an LBO event are presented in Figure 28. The most significant pressure reduction rate was observed to occur at  $x/H$  locations of 0.91, 5.74, and 6.82 at a time of 1610 ms from the start of the test sequence. The largest rate of pressure reduction occurred consistently at an  $x/H$  location of 6.82 for LBO tests with no discharge present. This axial location was therefore

determined to be suitable for detection of LBO onset. Pressure measured at  $x/H = 6.82$  was then used to begin synchronized discharge actuation and high-speed image acquisition. From repeated LBO tests without a discharge present, representative pressure thresholds selected for conditions prior to and after LBO onset were selected to be 75.8 kPa and 65.5 kPa, respectively.

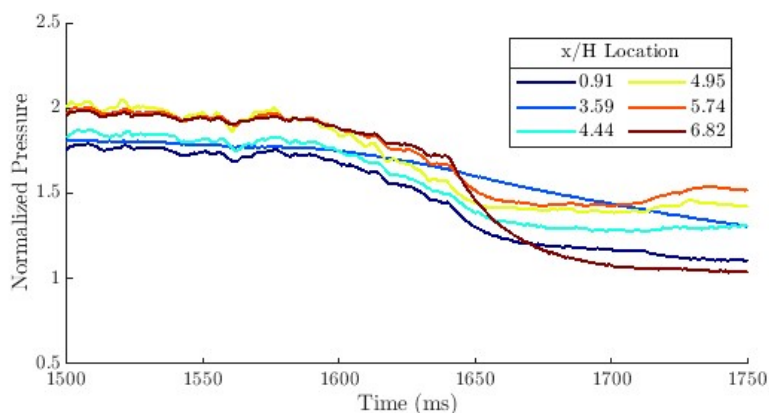


**Fig. 28:** Normalized pressure near the onset of a LBO event without discharge actuation. Pressure is normalized by the average facility nozzle exit pressure. Each line represents a different  $x/H$  location of measurement during the same test case. An  $x/H$  location of 6.82, just downstream of the cavity closeout, had the largest rate of change in pressure among all transducer locations.

Using these pressures as triggers to begin discharge actuation and data collection, three LBO events were averaged for each case with and without discharge actuation. Averaged pressure measurements for each event with and without the discharge were compared by subtracting the average without discharge actuation from the average with discharge actuation. Subtracted average contours over the combustor region are plotted in Figure 29 with discharge actuation after and before LBO onset on the left and right, respectively. Mean start times for discharge actuation were 242 ms and 1610 ms from the start of data collection for the before and after LBO onset cases, respectively. Corresponding standard deviations were 27.5 ms and 12.5 ms. When ns discharge actuation began prior to LBO, a noticeable difference in pressure retention is observed compared to LBO without a ns discharge. This extension of pressure retention, and thus the fuel-lean flameholding limit, is evident in the orange and red region downstream of the cavity closeout ramp ( $x/H \geq 6.82$ ). Discharge actuation after LBO onset showed less effectiveness compared to the before-LBO actuation case, but a positive effect was still observed downstream of the closeout ramp after LBO

onset. The improved combustor pressure retention with discharge actuation before an LBO event presents another utility of integrating a pulsed discharge system into a dual-mode combustor. An example of this utility may be locally increasing combustor pressure and maintaining a flame when local combustor equivalence ratio falls due to reduced fuel entrainment and mixing caused by non-uniform inflow. Future efforts in LBO comparisons with and without discharge actuation would ideally employ a longer, more continuous reduction in fuel mass flow rate than shown in Figure 26 and discharge actuation over a much longer time period (10s of seconds).

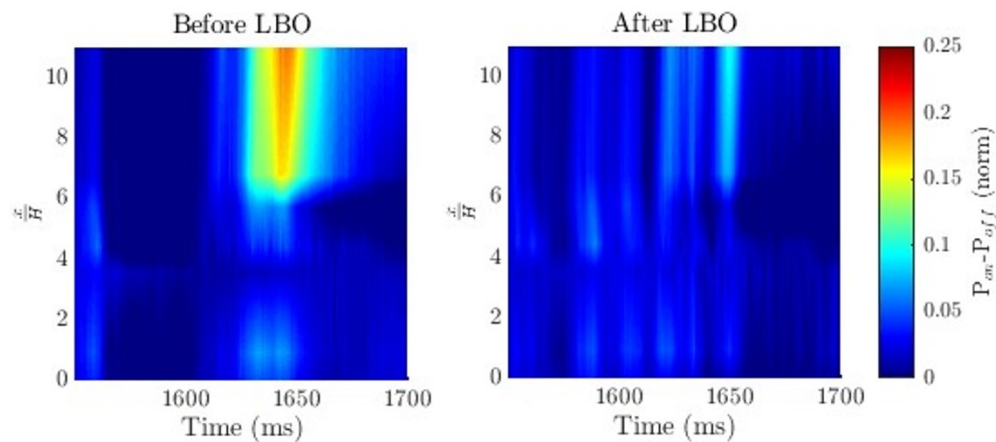


**Fig. 29:** Subtracted average (with discharge - without discharge) contour plots of 1 kHz pressure measurements over time downstream of the cavity leading edge. (Left) discharge actuation before LBO onset; (right) discharge actuation after LBO onset. Pressures were normalized by the average facility nozzle exit pressure across all LBO events. Discharge actuation prior to LBO showed increased pressure retention compared to discharge actuation after LBO onset.

## Appendix E: Ignition via Pulsed Nanosecond Discharge

Assessing extension of ignition capabilities relative to nominal UVASCF operation provides additional information on overall discharge utility. For ignition tests, ns discharge PRF was set to 50 or 100 kHz while flow stagnation temperature and air throttle actuation varied. Ignition success of the discharge is compared to backpressured ignition via hydrogen injection in Table 5. Variable parameters in discharge ignition attempts included stagnation temperature, discharge PRF, and added backpressure. For all ignition attempts with the discharge, fuel mass flow rate was held constant at 3.76 g/s. A designation of "AT" indicates a successful ignition attempt with added backpressure through air throttle actuation but no ignition without added backpressure. Discharge-assisted ignition, as expected, outperforms the conventional method of ignition by injection of hydrogen combined with added backpressure. Ignition was successful as low as 700 K with backpressure and as low as 1000 K without backpressure at a discharge PRF of 100 kHz. At a discharge PRF of 50 kHz with the same energy per pulse (a lower average power), ignition was only achieved at a stagnation temperature of 1200 K, indicating that the probability of ignition increases with an increase in PRF to 100 kHz. Previous works that have investigated scramjet cavity ignition via a repetitively-pulsed discharge [37] have noted that the increase of ignition probability with increased PRF can be attributed to an increased energy efficiency for ignition through enhanced inter-pulse coupling.

**Table 5:** Ignition success at different stagnation temperatures with an ethylene mass flow rate of 3.76 g/s (AT = successful ignition with air throttle, Yes = successful ignition, No = no ignition, "--" = not tested).

$T_0$ (K)	100 kHz Discharge	50 kHz Discharge	Hydrogen Pilot ( $x/H = 0.28$ )
700	AT	-	-
800	AT	-	-
900	-	No	-
1000	Yes	No	-
1100	Yes	No	-
1200	Yes	Yes	AT